

matvis: A matrix-based visibility simulator for fast forward modelling of many-element 21 cm arrays

Piyanat Kittiwisit ¹*, Steven G. Murray ^{2,3}, Hugh Garsden ^{4,5}, Philip Bull ^{5,1}, Christopher Cain ³, Aaron R. Parsons ⁶, Jackson Sipple⁶, Zara Abdurashidova⁶, Tyrone Adams⁷, James E. Aguirre ⁸, Paul Alexander⁹, Zaki S. Ali⁶, Rushelle Baartman⁷, Yanga Balfour⁷, Adam P. Beardsley ^{3,10}, Lindsay M. Berkhout ³, Gianni Bernardi ^{11,12,7}, Tashalee S. Billings⁸, Judd D. Bowman ³, Richard F. Bradley¹³, Jacob Burba ⁵, Steven Carey⁹, Chris L. Carilli ¹⁴, Kai-Feng Chen ^{15,16}, Carina Cheng⁶, Samir Choudhuri^{4,17}, David R. DeBoer ¹⁸, Eloy de Lera Acedo⁹, Matt Dexter¹⁸, Joshua S. Dillon ⁶, Scott Dynes¹⁵, Nico Eksteen⁷, John Ely⁹, Aaron Ewall-Wice ^{6,19}, Nicolas Fagnoni⁹, Randall Fritz⁷, Steven R. Furlanetto ²⁰, Kingsley Gale-Sides⁹, Bharat Kumar Gehlot³, Abhik Ghosh¹, Brian Glendenning²¹, Adelie Gorce²², Deepthi Gorthi ⁶, Bradley Greig ²³, Jasper Grobbelaar⁷, Ziyaad Halday⁷, Bryna J. Hazelton ^{24,25}, Jacqueline N. Hewitt ^{15,16}, Jack Hickish¹⁸, Tian Huang⁹, Daniel C. Jacobs ³, Alec Josaitis⁹, Austin Julius⁷, MacCalvin Kariseb⁷, Nicholas S. Kern ^{15,16,†}, Joshua Kerrigan ²⁶, Honggeun Kim ^{15,16}, Saul A. Kohn ⁸, Matthew Kolopanis ³, Adam Lanman²⁶, Paul La Plante ^{6,8}, Adrian Liu ^{6,22}, Anita Loots⁷, Yin-Zhe Ma ²⁷, David H. E. MacMahon¹⁸, Lourence Malan⁷, Cresshim Malgas⁷, Keith Malgas⁷, Bradley Marero⁷, Zachary E. Martinot⁸, Andrei Mesinger ², Mathakane Molewa⁷, Miguel F. Morales ²⁴, Tshegofalang Mosiane⁷, Abraham R. Neben ^{15,16}, Bojan Nikolic⁹, Chuneeta Devi Nunhokee ^{28,29}, Hans Nuwegeld⁷, Robert Pascua ^{6,22}, Nipanjana Patra ⁶, Samantha Pieterse⁷, Yuxiang Qin^{30,2}, Eleanor Rath^{15,16}, Nima Razavi-Ghods⁹, Daniel Riley¹⁵, James Robnett¹⁴, Kathryn Rosie⁷, Mario G. Santos^{7,1}, Peter Sims ²², Saurabh Singh ^{22,31}, Dara Storer²⁴, Hilton Swarts⁷, Jianrong Tan⁸, Nithyanandan Thyagarajan ^{32,14}, Pieter van Wyngaarden⁷, Peter K. G. Williams ^{33,34}, Zhilei Xu ¹⁵, Haoxuan Zheng¹⁶

Affiliations are listed in Appendix B.

Accepted XXX. Received YYY; in original form ZZZ

ABSTRACT

Detection of the faint 21 cm line emission from the Cosmic Dawn and Epoch of Reionisation will require not only exquisite control over instrumental calibration and systematics to achieve the necessary dynamic range of observations but also validation of analysis techniques to demonstrate their statistical properties and signal loss characteristics. A key ingredient in achieving this is the ability to perform high-fidelity simulations of the kinds of data that are produced by the large, many-element, radio interferometric arrays that have been purpose-built for these studies. The large scale of these arrays presents a computational challenge, as one must simulate a detailed sky and instrumental model across many hundreds of frequency channels, thousands of time samples, and tens of thousands of baselines for arrays with hundreds of antennas. In this paper, we present a fast matrix-based method for simulating radio interferometric measurements (visibilities) at the necessary scale. We achieve this through judicious use of primary beam interpolation, fast approximations for coordinate transforms, and a vectorised outer product to expand per-antenna quantities to per-baseline visibilities, coupled with standard parallelisation techniques. We validate the results of this method, implemented in the publicly-available `matvis` code, against a high-precision reference simulator, and explore its computational scaling on a variety of problems.

Key words: software: development, public release, simulations – algorithm – techniques: interferometric – cosmology: diffuse radiation, dark ages, reionization, first stars

* Email: piyanat.kittiwisit@gmail.com

1 INTRODUCTION

The 21 cm line emission from neutral hydrogen during the Cosmic Dawn and Epoch of Reionization is currently one of the most challenging observational targets for radio astronomers. According to theoretical models (e.g. [Cohen et al. 2018](#)), the total line emission is expected to be quite weak, on the order of tens to hundreds of mK, with fluctuations of $\Delta_{21}^2 \lesssim 10^3 \text{ mK}^2$ (where Δ_{21}^2 is the ‘dimensionless’ power spectrum at a given scale and redshift). In comparison, the Galactic synchrotron foreground emission is many orders of magnitude brighter, with a much larger variance ([Santos et al. 2005](#)). Contributions from extragalactic sources are also considerably brighter than the target 21 cm signal. As such, 21 cm surveys must achieve both high sensitivity, to reach an adequate signal-to-noise ratio to detect the 21 cm fluctuations, and excellent instrumental stability and calibration precision, in order to prevent spurious leakage of some fraction of the bright foregrounds into the 21 cm signal modes.

Even purpose-built 21 cm radio interferometer arrays have complex instrumental responses and systematics that interact with the sky and contribute to the difficulty of characterising the instrument sufficiently well to mitigate the foreground leakage problem mentioned above. These include the frequency- and direction-dependent polarised primary beam pattern of the antenna, and the time- and frequency-dependent receiver bandpass required to calibrate the data ([Barry et al. 2016](#); [Barry & Chokshi 2022](#)), the idiosyncratic properties of the receiver chain in the presence of radio frequency interference (RFI; [Wilensky et al. 2023](#)), environmental thermal variations ([Gehlot et al. 2021](#)), reflection and retransmission of signals over the air and through cables ([Kern et al. 2019, 2020](#); [Josaitis et al. 2022](#)), among others. In addition, the data analysis tools used to mitigate imperfections in the data (e.g. missing channels due to RFI contamination, filtering of cable reflections etc.) often have their own non-ideal behaviours, including the possibility of suppressing or filtering some of the 21 cm signal itself ([Cheng et al. 2018](#); [Kolopanis et al. 2019](#); [Pagano et al. 2023](#)).

Physical (electronic and mechanical) approaches to instrumental characterisation may be useful, but also have their limitations in terms of understanding the ultimate impact of these systematics on the processed data. For example, primary beams can be characterised through a variety of physical methods, including photogrammetry, overflights by drones carrying standard sources and so on, but may still fail to capture the precise shapes of far sidelobes with sufficient accuracy ([Jacobs et al. 2017](#)). Experimental approaches that isolate a single component of the system may also be unable to properly constrain the couplings and interactions between different components that give rise to some effects.

As a result, simulation-based approaches to study the complex process of observation and data analysis are now a vital part of all 21 cm experiments. An important advantage of simulations is that they can be used to develop increasingly complex ‘what if’ scenarios for the systematic effects that are identified, particularly for effects that would be close to (or even below) the noise level of the available data. Simulations can also be used as part of holistic efforts to ‘validate’ the data analysis pipeline, allowing analysts to explicitly determine levels of signal loss or other spurious features in the processing of the data as each step of the pipeline proceeds ([Aguirre et al. 2022](#)). A disadvantage of simulation-based approaches is that they require models to be available for each system component, each systematic effect, and indeed the sources of emission on the sky, which can lack realism. They can also be computationally expensive, particularly when simulations for the whole array are required – not only must we run the data analysis pipeline on a large volume of

simulated data but we must also generate and store the simulated data itself.

A wide range of approaches have been taken with regards to simulating the complex visibilities measured by radio interferometer arrays. Existing packages include: OSKAR ([Mort et al. 2010](#)), RIMEz ([Martinot 2022](#)), `pyuvsim` ([Lanman et al. 2019](#)), `healvis` ([Lanman & Kern 2019](#)), MeqTrees ([Noordam & Smirnov 2010](#)), Montblanc ([Perkins et al. 2015](#)), FHD ([Sullivan et al. 2012](#)), WODEN ([Sullivan et al. 2012](#)), and CASA ([THE CASA TEAM et al. in press](#)). These vary significantly in realism, performance, and importantly accuracy. The basis of most visibility simulators is generally a suitable simplification or special case of the radio interferometric measurement equation (RIME; [Price & Smirnov 2015](#)). The realism of the simulations is largely governed by the realism of the models used for each component of the system that is modelled by the RIME, such as the primary beam response, the sky intensity distribution, and the array layout. Further instrumental and observational effects are usually added on top of the RIME as post-processing steps; there is no need to simulate RFI pulses through the visibility simulator machinery in most cases, for example. The performance of the simulators is governed by a few factors: the scale of the simulation, the particular choices of the algorithms and technology used to implement the RIME, and the approximations that are used in evaluating the RIME and its constituent component models. For instance, simulating ‘realistic’ data volumes of a very large array, consisting of many antennas with wideband receivers, observing for a potentially very long period of time, can soon become prohibitively expensive, especially if multiple runs (e.g. to model different scenarios) are required. The performance of such a simulation can often be improved by employing parallelisation, vectorisation or GPU acceleration.

One may also utilise approximations, such as analytical forms of the sky intensity and primary beam response that can be evaluated quickly, to improve performance at the cost of realism. These approximations can also be important sources of inaccuracy. No simulator will be perfectly accurate, given limits to numerical precision and the uncertainty in the models of different components, but certain choices of algorithm and functional basis can give rise to inaccuracies that can potentially exceed the size of the effects that one is trying to model. Balancing realism, performance and accuracy can be complicated and depend on specific use cases. Regardless, it is important that the impact of the approximations and the overall accuracy of the simulator is well understood, validated, and documented for users, particularly when the simulation will be used to validate highly sensitive analyses of real data.

In this paper, we introduce the `matvis` visibility simulator and conduct rudimentary validation of its outputs. `matvis` has been designed to perform fast simulations of the response of many-element 21 cm arrays at low frequency, in particular the Hydrogen Epoch of Reionization Array (HERA), although the underlying architecture of the simulator is more general and applicable to any radio interferometric array at any frequency. To meet the performance requirements to simulate extremely large HERA observations, `matvis` employs a matrix-based approach to evaluate the RIME, which is able to naturally take advantage of GPU acceleration. The primary novelty of `matvis` is that it treats the RIME as an outer product over antennas, enabling the RIME for all baselines and polarisations at a single time and frequency to be computed as a single matrix product. The discretisation of the sky required to enable this matrix-based approach is predicated on being able to treat local equal-solid-angle ‘pixels’ as delta-function point sources, essentially approximating the RIME angular integral as a Riemann sum (in the same way as `pyuvsim`, for example). A further novelty (and approximation) of `matvis` is that it

utilises a coordinate transformation scheme that combines accurate-but-slow *astropy* (Astropy Collaboration et al. 2013, 2018, 2022) algorithms with simple-and-fast trigonometric-based calculations to significantly improve computational performance (for simulations requiring multiple time-snapshots) with minimal impact on accuracy.

We describe the *matvis* algorithm along with the approximations and assumptions that we have made in Section 2. Section 3 describes the software aspects of the publicly available *matvis* package hosted on GitHub. In Section 4, we perform a rudimentary ‘validation’ of *matvis* against *pyuvsim*, an alternative simulator that has been designed to carefully and correctly evaluate each step of the RIME, at the cost of decreased computational performance. We explore effects of *matvis* coordinate transformation scheme and show that *matvis* can attain accuracy comparable to *pyuvsim*. We also demonstrate the limitation of the point-like sky assumption in this section. Lastly, we study the computational scaling of *matvis* to understand its performance in simulating ever-growing data sets on large arrays in Section 5 and conclude in Section 6.

2 COMPUTATIONAL SCHEME

In this section, we introduce the algorithm used by *matvis* to simulate visibilities. In common with all visibility simulators, a variety of choices need to be made in terms of how to model the sky (particularly whether and how to decompose it into a set of discrete elements); how to perform the integral over the whole sky required by the radio interferometer measurement equation (RIME); how to model the primary beams of the antenna elements; what coordinate systems to work in; and how to approximate or optimise computationally demanding steps of the process.

2.1 Basic Framework

The purpose of the visibility simulation is to evaluate some form of the RIME (e.g. Hamaker et al. 1996; Smirnov 2011) at the desired frequencies and observing times for a given sky model and instrumental model. Let Ω be celestial coordinates for a point on the sky (e.g. equatorial coordinates in RA and DEC); then the RIME for a snapshot visibility (at a particular time t , and frequency ν) can be written in a reasonably general form as (Kohn et al. 2019)

$$V_{ij}(\nu, t) = \int_{4\pi} \mathbf{A}_i(\nu, t) \mathbf{C}(\nu) \mathbf{A}_j^\dagger(\nu, t) \exp(-2\pi\nu i \mathbf{b}_{ij} \cdot \mathbf{n}/c) d^2\Omega. \quad (1)$$

Here, V_{ij} is the complex visibility for a baseline formed from antennas i and j , and we have suppressed dependence on sky coordinate inside the \mathbf{A} and \mathbf{C} terms in the integral for notational clarity. In this expression, \mathbf{A}_i denotes the polarised primary (E -field) beam for antenna i , also known as the direction-dependent Jones matrix. \mathbf{A}_i is an $N_{\text{feed}} \times 2$ matrix, whose components are the antenna patterns for each polarisation feed p , and two unit vectors needed to mode the response to an incident E -field from spherical polar direction $k \in (\theta, \phi)$. Throughout, we will assume the case in which $p \in \{X, Y\}$, i.e. in which there are two perpendicular polarisation feeds, though *matvis* trivially deals with the case in which there is a single feed. Since we have chosen to represent the RIME integral as an integral over celestial coordinates, \mathbf{A} is represented as evolving over time, as the earth rotates. \mathbf{C} denotes the coherence matrix, which models the polarised flux distribution on the sky, which we

assume is static in celestial coordinates.¹ Finally, the exponential term, which shapes the fringe pattern of the radio interferometer, includes a scalar product between the baseline vector \mathbf{b}_{ij} connecting the antennas, and a unit vector \mathbf{n} towards a particular point on the sky. The integral over solid angle is performed over 4π steradians, so that in principle the whole sky contributes to each complex visibility. In practice, only emission above the horizon at any particular time actually contributes, and this ‘horizon cutoff’ can be bundled into the primary beam².

From here, all visibility simulators must make at least one approximation: we must make a choice about which discrete basis the sky model should be represented in, so that the integral in Equation 1 can be discretised. This is due to the fact that we do not have analytic forms of the sky or primary beam model as a function of sky coordinate. A very natural basis is a ‘pixelisation’, i.e. a choice of a set of points on the sky to which we assign the total intensity from their surrounding local region, and this is the representation that *matvis* adopts. Note that while this form of ‘pixelisation’ is natural, it is by no means the only one. Discretisations in other kinds of bases exist, for example spherical harmonics (Martinot 2022).

Furthermore, *matvis* makes a slightly more stringent ‘point-source approximation’ for each sky pixel (Lanman et al. 2022); it explicitly assumes that the full flux from a given region that encompasses a pixel really does come from an infinitesimal point source located within the region, at which the primary beam and fringe term are evaluated. This point-source representation is in fact perfect if the sky purely consists of unresolved point-sources. However, if the sky contains pixelisation of extended sources, it will inherently miss fluctuations on scales smaller than the pixel size. In principle, this limitation can be overcome by ‘over-sampling,’ i.e. providing a higher-density array of input pixels at which the beam and the fringe pattern can be evaluated, but this can be tricky to accomplish in practice as we will demonstrate in Section 4.2.

Summarily, *matvis* uses a ‘point source’ representation, treating the sky as a set of point sources with arbitrary frequency spectra binned into discrete frequency channels. It does not enforce any particular ‘pixelisation’, other than the condition that the sum of all pixel intensities equals the total intensity of the sky. A common example of such a pixelisation for diffuse emission is HEALPIX³ (Górski et al. 2005), but we emphasise that *matvis* does not require a HEALPIX representation, or even an equal-area pixel decomposition.

From here on, we will refer to each component of the sky as a ‘source’ or ‘point source’ with the understanding that it may either be a truly physical point source, or an approximation of a region of solid angle as such. For a point source n at equatorial coordinates $\theta_{\text{eq}}^{(n)}$, the coherency matrix in frequency channel a is given by

$$\mathbf{C}_{pq}^{(n)}(\nu_a, \theta_{\text{eq}}^{(n)}) = \delta^2(\theta_{\text{eq}} - \theta_{\text{eq}}^{(n)}) f_{pq}^{(n)}(\nu_a), \quad (2)$$

where $f_{pq}^{(n)}(\nu_a)$ is the source SED for the polarisation pq (eg. XX), evaluated at the centre frequencies of the discrete frequency channels, and the 2D Kronecker delta function has its usual meaning.

¹ Of course, we could have represented the RIME in topocentric coordinates, in which case \mathbf{A} would have been static, and \mathbf{C} would evolve, but this representation is conceptually simpler for our algorithm presented later.

² The approach of bundling horizon effects into the beam is actually useful in terms of implementation because in practice the horizon may not always be perfectly flat (Bassett et al. 2021), and therefore should be left flexible for a user to modify.

³ <http://healpix.sf.net/>

With our explicit assumption of a point-like sky model in place, we can write the RIME, at a particular frequency, as

$$V_{ij}^{pq}(v_a, t) = \sum_n A_i^p(v_a, \theta_{\text{hrz}}^{(n)}(t)) \cdot A_j^{q*}(v_a, \theta_{\text{hrz}}^{(n)}(t)) \times \mathbf{C}_{pq}^{(n)}(v_a, \theta_{\text{eq}}^{(n)}) \exp\left(-2\pi i v_a \tau_{ij}^{(n)}\right). \quad (3)$$

This gives the complex visibility V_{ij}^{pq} for antenna pair i, j and polarisation pq . The sum is over all point sources in the sky model. A_i^p is the complex primary beam response for antenna i on feed p , and is a length-2 vector representing the response in the azimuth and elevation directions. The primary beam is evaluated at $\theta_{\text{hrz}}^{(n)}(t)$, the apparent angular position of each point source n in a horizontal (topocentric) coordinate system at time t . The phase factor is a function of a baseline- and source position-dependent delay,

$$\tau_{ij}^{(n)} = \mathbf{X}_{\text{hrz}}^{(n)}(t) \cdot \mathbf{b}_{ij}/c, \quad (4)$$

where $\mathbf{X}_{\text{hrz}}^{(n)}(t)$ is the Cartesian unit vector pointing towards the source at an observed time t in the same horizontal coordinate system as the baseline vector \mathbf{b}_{ij} between the centres of antennas i and j , and c is the speed of light. We note that \times here indicates scalar multiplication (from the product of $A_i^p \cdot A_j^{q*}$) to \mathbf{C} , and we have chosen to write the source position unit vectors in the coordinate frames and representations that are more practical to evaluate for the different terms. We also note that the only approximation made in arriving at Equation 3 has been the ‘point source approximation’ that discretises the spatial integral.

2.2 Matrix-Based Computation of the RIME

To obtain the visibilities, Equation 3 must be calculated for all discrete frequencies, and at all requested discrete times, for all antenna pairs i, j . This becomes computationally prohibitive for large arrays. For reference, the completed HERA array will have 350 antennas (up to $\approx 61,000$ baselines), 1535 frequency channels, and so observing with a ≈ 10 sec cadence over, say, 8 hours per night, we can see that Equation 3 must be evaluated around $\sim 2.7 \times 10^{11}$ times to simulate even a single night of observing in full. Multiplying this by the number of individual sources in the sky model (e.g. the $\approx 300,000$ point sources in the GLEAM catalogue), this grows to $\sim 8 \times 10^{17}$. Clearly, the computational problem is large in scale.

A possible direction for optimisation is to notice that some of the terms in Equation 3 only need to be evaluated once for each antenna and point source at a given time and frequency. For example, a somewhat expensive conversion from equatorial to horizontal coordinates, followed by another expensive evaluation of the primary beam interpolation function, is needed to evaluate the primary beam factor at each point source at each observing local sidereal time (LST). This conversion is common to all frequencies, and only needs to be done per antenna rather than per baseline.

At this point, we introduce a computational trick that allows Equation 3 (and by extension Equation 4), which are defined per baseline, to be rewritten as an outer product of two vectors that are defined per antenna only. The outer product ‘expands’ the calculated quantities into a full set of cross-correlations for all baselines. This significantly reduces the number of repeated calculations, especially for a large array, and makes good use of the vectorisation capabilities of the `numpy` library (and modern CPUs). The downside is that all antenna-antenna correlations must be performed to make use of this trick, so it is not possible to be selective about which baselines are formed. For problems where the number of baselines to be simulated is close to

the maximum for the array, $N_{\text{bls}} \approx N_{\text{ants}}(N_{\text{ants}} - 1)/2$, this approach will be highly efficient.

To implement this trick, let $A_{ip}^{nk}(v_a, t)$ be the complex response of antenna i on feed p to source n in the E -field direction k , and define the per-antenna quantity,

$$z_{ip}^{nk}(v_a, t) = A_{ip}^{nk}(v_a, t) \sqrt{\mathbf{C}_{pp}^{(n)}(v_a)} \exp\left(-2\pi i v_a \mathbf{X}_{\text{hrz}}^{(n)}(t) \cdot \mathbf{x}_i/c\right), \quad (5)$$

where \mathbf{x}_i is the position vector of antenna i in horizontal coordinates. We have noted the dependence on frequency and time for each term in this equation rather than include discrete frequencies and times in the indices for each quantity; this indicates that these vectors are evaluated per frequency and per time, and the calculation may be parallelised over these dimensions (placing frequency and time as the outermost loops of the algorithm). The visibility (Equation 3) can then be written

$$V_{ij}^{pq}(v_a, t) = \sum_{k,n} z_{ip}^{nk} \left(z_{jq}^{nk}\right)^\dagger, \quad (6)$$

noting that the RHS is simply a matrix product $\mathbf{Z}\mathbf{Z}^\dagger$ if \mathbf{Z} is written as a matrix form of z , whose rows contain all antennas and feeds, and whose columns contain all sources and E -field vectors. The matrix product produces the necessary two beam factors (with the Hermitian conjugate), squares the square root of the coherency matrix, and forms the necessary phase factor as

$$e^{-iy \cdot \mathbf{x}_i} e^{-iy \cdot \mathbf{x}_j} = e^{-iy \cdot (\mathbf{x}_i - \mathbf{x}_j)} = e^{-iy \cdot \mathbf{b}_{ij}}, \quad (7)$$

where we have defined $\mathbf{y} \equiv 2\pi v_a \mathbf{X}_{\text{hrz}}^{(n)}(t)/c$ for compactness.

There are a few important observations to be made about this trick. First, we note that we have only used \mathbf{C}_{pp} , and never the cross-polarisation \mathbf{C}_{pq} of the sky model. This is due to the requirement of using the square root of the coherency matrix terms, which are essentially always positive for XX and YY but may be negative for the cross-terms in a small number of situations. In practice, the current incarnation of `matvis` uses only the total sky emission, assumed to be split evenly between XX and YY polarizations. Simulating the total flux from the sky should always allow this condition to be satisfied however. Secondly, note that the peak memory usage for this algorithm is almost completely controlled by the number of antennas and feeds, as they are combined as an outer product. Both frequency and time are neither summed over nor interact with other frequencies and times, making them ideal as outer-loops for the algorithm. The source and field-component axes are summed over, and therefore may be ‘chunked’ to suit any memory needs, at the expense of some vectorisation. Thirdly, the formulation of Equation 6 requires that all baselines are simulated at once. This can be a disadvantage when simulating arrays with high number of redundancies although the optimisation implemented here still leads to several orders of magnitude speed up in comparison to a simulator that directly evaluates per-baseline visibilities in Equation 3 such as `pyuvsim` (see Section 5). Nevertheless, we believe that further optimisation to this algorithm is possible, and we describe the idea in Appendix A to be fleshed out in future work.

2.3 Coordinate transformations

One of the key contributors to the accuracy of a visibility simulator, as well as its computational performance, is the manner in which the necessary coordinate transformations are carried out. On the one hand there is a sky model, which is most naturally represented in a

celestial coordinate system, e.g. equatorial coordinates. On the other, there are the instrumental terms, particularly the primary beam response and the set of baseline vectors, which are most naturally represented in a horizontal coordinate system connected to the location of the array. The complex exponential (fringe pattern) term in the RIME mixes the two, as it involves both the source position and baseline vectors. It is therefore always necessary to transform between celestial and horizontal coordinates at some point in the RIME calculation.

One way to perform these coordinate transforms is to use simplified trigonometric calculations that (i) converts from equatorial (RA and Dec, α and δ) coordinates to a Cartesian system, and then (ii) performs a solid body rotation into a horizontal coordinate system. The first step is,

$$\mathbf{X}_{\text{eq}}^{(n)} = \left(\cos \alpha^{(n)} \cos \delta^{(n)}, \sin \alpha^{(n)} \cos \delta^{(n)}, \sin \delta^{(n)} \right). \quad (8)$$

This vector of coordinates only needs to be calculated once for each source n in the catalogue. The rotation matrix for (ii) is the same for all point sources for a given LST, and so there is also a computational saving from only needing to calculate it once per LST. Defining the horizontal coordinate system as an ENU (East-North-Up) topocentric system, we obtain the rotation matrix,

$$\mathbf{R}(t) = \begin{pmatrix} \sin(H) & \cos(H) & 0 \\ -\sin(l) \cos(H) & \sin(l) \sin(H) & \cos(l) \\ \cos(l) \cos(H) & -\cos(l) \sin(H) & \sin(l) \end{pmatrix}, \quad (9)$$

where H is the hour angle of a reference point on the celestial sphere as a function of LST, and l is the latitude of the array on the Earth.

Although this is fast, as it relies only on basic operations, and can be used to give a reasonable representation of the necessary coordinate transformations, it is also inaccurate owing to the lack of astrometric corrections. A number of time-dependent corrections for precession, aberration, and so on, are generally required to recover the apparent positions of celestial sources within arcsecond accuracy. In the case of `matvis`, the fringe term, i.e. the exponent term in Equation 5 which requires time-dependent source positions in horizontal coordinates, is particularly sensitive to positional errors, and we have found in our tests that the accuracy of the equatorial-to-horizontal coordinate transform is often the main driver of the precision of the simulator as a result. The easy solution is to use `astropy` as a full set of astrometric corrections has been implemented in its coordinate transformation module. However, these corrections can be expensive to compute, particularly for large catalogues containing many sources, and we have found that employing a full `astropy`-based coordinate transforms significantly limits the performance of `matvis`.

As such, we implement a two-step coordinate transformation scheme, which in our case are applied to the point sources, to find their locations in Cartesian horizontal coordinates at each LST. In short, we perform a pre-computation procedure to ‘perturb’ the input equatorial coordinates of the sources so that steps (i) and (ii) in the trigonometric transforms (i.e. Equation 8 and 9) result in a more accurate observed source location when applied. These fictitious coordinates only need to be computed once, and significantly improve the accuracy of the results. To compute them, we simply use `astropy` to do the (more precise, but slower) equatorial-to-horizontal coordinate conversion for all sources at a single ‘reference time,’ given in Julian Date (JD), and then apply the inverse operations for steps (ii) and (i) to calculate a set of perturbed equatorial coordinates of the sources. When steps (i) and (ii) are subsequently applied to the perturbed coordinates for other LSTs, we find a significant improvement to the accuracy of the observed source locations compared with

the unperturbed ones. This correction degrades with increasing separation in time from the LST corresponding to the reference time although it will improve again once the separation is larger than ≈ 12 h, and reach the best improvement again at slightly less than 24 h from the reference time, because the correction is tied to the source positions. We study the accuracy of this approach in more detail in Sect. 4.1.

2.4 Beam Interpolation

One of the most important factors in the accuracy of the simulator is how accurately the antenna beams are represented. This is made more complicated by the fact that the beams must be evaluated at floating sky-coordinates defined by the discrete sky sources, as they drift in time. `matvis` allows two main forms of antenna beam to be input: analytic beams, and simulated beams. The former are easily evaluated at any coordinate (and frequency) by their nature, and typically in a very efficient manner. The latter presents more challenges; simulated beams are typically simulated on a discrete angular grid that cannot coincide with the floating sky-coordinates at which the beam must be evaluated. Therefore, they must be interpolated.

`matvis` makes use of the `UVBeam` class from the `pyuvdata` package (Hazelton et al. 2017), developed and maintained by the Radio Astronomy Software Group (RASG⁴), to handle the beam information and interpolation of regularly gridded, HEALPix gridded, and CST-simulated beams. The interpolation is selectable as it uses `numpy.RectBivariateSpline` internally. For example, this can be bilinear, bicubic, or quintic, on a regular grid of altitude and azimuth. The bilinear form is easy to match with an algorithm that utilises the blazing-fast linear interpolation capabilities of GPUs and, based on our testing, provide sufficient accuracy for our specific use case of simulating mock data to validate the HERA pipeline. For other use cases that require higher accuracy, such as simulating a visibility model for calibration, higher-order forms of interpolation should be used. One point to note concerning this interpolation is that it is essential that the regular coordinates of the simulated lattice be defined on a spherical grid which has the zenith as a pole. This is due to the fact that many common E -field beam responses have a discontinuity in their phase (recalling that the response is complex) for one of their components at zenith, which is properly interpolated only if the zenith is considered a pole and interpolated ‘away from’.

We describe how the beam information (as well as other required inputs) are passed to `matvis` in the next Section.

2.5 Summary of Algorithm

Having described the mathematical framework in the preceding sections, we now summarise the algorithm of `matvis` as it stands in its present implementation⁵.

Firstly, we note that each step is to be performed at a single frequency. Thus, frequency forms our outer-most loop, and indeed it is envisaged that each frequency would typically be performed as a separate job on a high-performance computing scheduler, i.e. as an *embarrassingly* parallel task. Our second, internal, loop is over times.

The following inputs are expected by the basic `matvis` algorithm:

⁴ <https://radioastronomysoftwaregroup.github.io/>

⁵ That is version 1.1.0 at the time of the publication of this article.

- A set of antenna locations, $\mathbf{D} = \{\mathbf{x}_1, \dots, \mathbf{x}_{N_{\text{ants}}}\}$ in Cartesian East-North-Up (ENU) coordinates as an $N_{\text{ant}} \times 3$ matrix.
- A beam model, $A_{ijk}(v, \theta)$ for each *unique* antenna, i , feed j and E -field component $k \in (\theta, \phi)$, that may be evaluated (or interpolated) to any particular set of topocentric coordinates. Note that two physically separate antennas that nevertheless are assumed to have the same beam need only be provided once.
- An integer-valued vector a_i whose value for antenna i is the index of its corresponding beam model, i .
- A matrix of sky model source locations in Cartesian equatorial coordinates (ECD), $\mathbf{X}_{\text{eq}} = \{\mathbf{X}_{\text{eq}}^{(0)}, \dots, \mathbf{X}_{\text{eq}}^{(N_{\text{src}})}\} \in \mathbb{R}^{3 \times N_{\text{src}}}$, where each source is given by Equation 8.
- A positive, real-valued vector of source intensities, $\mathbf{I} \in \mathbb{R}_+^{N_{\text{src}}}$, where $\mathbf{I}_n = 2\mathbf{C}_{00}^{(n)} = 2\mathbf{C}_{11}^{(n)}$.
- An array \mathbf{R} of shape $N_{\text{times}} \times 3 \times 3$ containing the rotation-matrices (cf. Equation 9) required to convert from equatorial to topocentric coordinates at each time-step. These are computed *outside* the main algorithm loop using any method the user desires (though utilities for computing these are provided in the package). These matrices also *define* the times of the simulation (no other time information is given to the algorithm).

Then, for a particular frequency ν and time-index t , the `matvis` algorithm performs the following:

- (i) Rotate the pixels/sources above the horizon into topocentric frame: $\mathbf{X}_{\text{hrz}} = \mathbf{R}_t \mathbf{X}_{\text{eq}}$.
- (ii) Interpolate the beams onto source coordinates, i.e. produce the $N_{\text{beam}} N_{\text{feed}} \times N_{\text{ax}} N_{\text{src}}$ complex-valued matrix $\mathbf{A}_{ij,kl} = A_{ijk}(v, \mathbf{X}_{\text{hrz}}^{(l)})$ for unique antenna beam i , feed j , E -field component k and source l .
- (iii) Compute the antenna-based exponent: $\tau = -2\pi i \nu \mathbf{D} \mathbf{X}_{\text{hrz}} / c$, which is an $N_{\text{ant}} \times N_{\text{src}}$ matrix.
- (iv) Compute the $N_{\text{ant}} N_{\text{feed}} \times N_{\text{ax}} N_{\text{src}}$ per-antenna complex-valued matrix $\mathbf{Z}_{ij,kl} = \sqrt{\mathbf{I}_l} \mathbf{A}_{a_i j,kl} \exp(\tau_{il})$, the matrix form of Equation 5.
- (v) Compute the $N_{\text{ant}} N_{\text{feed}} \times N_{\text{ant}} N_{\text{feed}}$ visibility: $\mathbf{V} = \mathbf{Z} \mathbf{Z}^\dagger$ (Equation 6).

There are a few important details to note with respect to this algorithm. First, the present implementation of this algorithm only allows simulating drift-scanning observations, which is the common observing mode of 21 cm cosmology experiments such as HERA. This limitation is due to the fact that the algorithm simply evolves the input source matrix by making a horizontal cut and then computing the visibilities from all sources that are rising for each iteration in time. To enable tracking observation, an additional step that rephases the output visibilities to a given phase centre would need to be implemented.

Secondly, since steps (iv) and (v) are simply matrix products, highly efficient thread-optimised implementations exist to compute them on CPUs, eg. in BLAS⁶. Furthermore, drop-in replacements exist to compute matrix products even more efficiently on GPUs, for example the CUBLAS package. This is highly advantageous, as step (vi) is the computation bottleneck for realistic modern large- N arrays.

Lastly, the beam interpolation in step (ii) need only be performed for the number of *unique* antenna beams. In many cases of current interest, all antennas will be assumed to have the same beam, which makes this step negligible in terms of computation. Nevertheless,

if the simulation is intended to capture beam irregularities across the antennas, this step can become highly non-negligible. However, GPUs are also extremely well-adapted to spatial interpolation; thus a well-tuned GPU implementation, e.g. by using texture mapping, can significantly reduce this cost.

3 THE `matvis` PACKAGE

The `matvis` package defines an API and an algorithm for computing the RIME, with the intention that different implementations can be provided as drop-in replacements of each other. Currently, the package provides two such implementations: `matvis.cpu` and `matvis.gpu`, which define CPU-based and GPU-based implementations respectively. Notably, the API computes the RIME at a single frequency only but includes a loop over time. The majority of the code (all of the CPU-based implementation) are written in pure Python, utilising the standard `numpy`, `scipy`, and `astropy` libraries. The GPU-based implementation replaces some of the `numpy` operations, particularly steps (ii)-(v) (as described in Section 2.5), with CUDA code wrapped by PyCUDA. Each step of the algorithm is implemented as its own CUDA kernel, glued together in Python to maintain code simplicity. Notably, matrix products directly use the highly-optimised cuBLAS library.

To maintain feature parity between the CPU-based and GPU-based implementations, the coordinate transformation scheme outlined in Section 2.3 is separately implemented in the function `equatorial_to_eci_coords` in the `conversions` module of the Python package because a GPU-based `astropy` coordinate transformation module does not exist. Users can manually call this function to put sources into the ‘perturbed’ equatorial coordinates (as described in Section 2.3) before passing them to the main `matvis` routine to improve accuracy of the coordinate rotation in step (i). Although this is not required, i.e. the API has no knowledge of whether this correction has been applied, we highly advise that all simulations use it (see Section 4.1.1 on how this influence the simulation outputs).

As discussed, interfacing and interpolation of gridded beams are handled by the `UVBeam` from the `pyuvdata` package developed and maintained by RASG. For analytic beams, uniform, Gaussian, and Airy beams are readily supported through the `AnalyticBeam` class of the `pyuvsim` package, which is also developed and maintained by RASG, and shares a common beam evaluation interface with the `UVBeam` interpolation. Other forms of analytic beams are possible by sub-classing the `AnalyticBeam` class, one of which that we have developed is the `PolyBeam` class in the `hera_sim` package, which implements an analytical model of the HERA Phase I primary beam (Choudhuri et al. 2021, see Section 3).

A high-level wrapper is available via the `simulate_vis` routine, which provides a loop over frequencies, as well as simple implementations to compute the required input equatorial sky coordinates, \mathbf{X}_{eq} from the more common RA/DEC. This high-level wrapper also provides a simple switch between different back-end implementations (i.e. CPU and GPU). We note that this wrapper does *not* provide in-built capability to perform the coordinate perturbations (though pre-perturbed coordinates can be computed and provided to the wrapper by using the above mentioned function).

A separate wrapper is also available via the `visibilities` module in the `hera_sim` package, a simulation package for HERA-like redundant interferometric arrays, also developed by the HERA collaboration. This has a few key advantages over the in-built wrapper in the `matvis` package, including an option to apply coordinate correction given a reference time, a unified simulation interface that

⁶ Basic Linear Algebra Subroutines: <https://www.netlib.org/blas/>.

can be used to wrap other simulator codes (with `pyuvsim` wrapper already implemented), and integration with systematics models available in the `hera_sim` package. The main script of this wrapper, `hera-sim-vis.py`, uses `pyuvsim`-style configuration files⁷, making it much easier to configure and execute a large set of simulations on an HPC cluster. The `hera_sim` package also implements an analytical model of the Phase I HERA dipole beam (Choudhuri et al. 2021) in its `PolyBeam` class for use with `matvis` (and `pyuvsim`) although we note that the `pyuvsim`-style configuration files do not currently support this beam (or any analytic beam models implemented outside of the `AnalyticBeam` class of the `pyuvsim` package), and thus users must manually build `matvis` simulations via the `hera_sim` unified interface to use this beam.

The `matvis` package⁸ and all of its associated software that we have mentioned in this paper, including `hera_sim`⁹, `pyuvsim`¹⁰, and `pyuvdata`¹¹, are publicly available via open-source licenses on GitHub. PyPI distributions are also available, allowing easy installation via the `pip install` command. `matvis` has been under active development since May 2021. The development cycle employs `git` and GitHub and strictly follows an open-source development guideline laid out by the HERA collaboration¹². Particularly, we adopt continuous development and comprehensive code review processes, thorough unit-testing, including for `pyuvsim` and `pyuvdata`, and maintain detailed and user-friendly documentation¹³, including both API-level ‘docstrings’ and a set of tutorials. We use Continuous integration (CI) to run tests and report coverage. Although the primary contributions to the `matvis` code have thus far come from members of the HERA collaboration, we welcome and appreciate contributions from outside of the collaboration.

4 VALIDATION

In this section, we validate `matvis` against a reference implementation of the RIME in the `pyuvsim` visibility simulator (Lanman et al. 2019). Both `matvis` and `pyuvsim` assume the point-source approximation for sky models and use E -field primary beams (interpolated to given source positions and frequencies) in the calculations. The main differences are that `pyuvsim` (i) directly calculates a full Jones-matrix contribution (Hamaker 2006) from each point source to each baseline, and (ii) uses `astropy` for coordinate transformation, providing the best possible source position accuracy. In contrast, `matvis` uses (i) a matrix-based optimisation to trade the possibility of simulating from fully polarised sky models for speed, and (ii) a coordinate transformation scheme in place of `astropy` to trade some accuracy for speed. However, we will show that the outputs from `matvis` are, on average, comparable to `pyuvsim` to within < 0.5 percent in amplitude, and $< 0.3^\circ$ in phase.

We perform two validation tests. First, we simulate drift-scan observations from a point-source catalogue with both simulators and compare the results. An unresolved point source, given its position and integrated flux, is already in an ideal discrete basis under the

point-source approximation. Thus, this test should provide a clean comparison of the accuracy between the two simulators. Effects from the `matvis` source position correction are also demonstrated here. Then, we simulate from a pixelised map of a diffuse sky model. In addition to comparing the accuracy of the simulators, we will also demonstrate limiting factors of the pixelised sky map, which is inherent to the point-source approximation that is being used by both `matvis` and `pyuvsim`. All simulations are performed in double precision on the CPU implementation of the code, and all results shown are from the ‘xx’ polarisation. The coordinate transformation described in Section 2.3 is applied to all `matvis` simulations.

The following software versions are used throughout these tests: `matvis==1.2.1`, `hera_sim==4.2.0`, `pyuvsim==1.2.6`, and `pyuvdata==2.4.0`. We note that the results presented here should be treated as a rudimentary validation and demonstration of `matvis`, not an absolute measure of its accuracy. The numbers will change depending on the simulation parameters, and whether they are sufficiently accurate enough will depend on specific use-cases.

4.1 Point Source Simulation

We begin by taking the 100 brightest point sources from the Galactic and Extra-Galactic All-Sky MWA survey (GLEAM; Hurley-Walker et al. 2017) catalogue and adding the 9 very brightest sources that were peeled from it (as given in Table 2 of the cited paper). We also add a single point-source model of Fornax A with a flux of 750 Jy and spectral index of -0.825 at a right ascension of 3h22m42s and a declination of $-37^\circ 12' 2''$ (McKinley et al. 2015), giving a total of 110 sources. We simulate zenith-pointing, drift-scanning, observations with both `matvis` and `pyuvsim` from this mock catalogue at 100 MHz, 10 kHz channel width, over 24-h LST with 10-s integration (JD 2458101.2115–2458102.2114, 8640 time steps in total). The telescope layout is taken from the HERA array (Latitude -30.7215° , Longitude 21.4283°), which consists of 350 14-m parabolic dishes; 331 of which are densely packed into the hexagon ‘core’ while the rest of the antennas form the ‘outriggers’ around the core, providing longer baselines for some imaging capability (Dillon & Parsons 2016). We simulate several East-West and North-South aligned (hereafter E-W and N-S) baselines in the HERA array layout, specifically 14, 292, 584, and 876 m for the former and 25, 245, 460, and 742 m for latter. For each direction, these set of baselines roughly correspond to: the shortest baseline in the core, the longest baseline in the core, the longest baseline from the core to the outriggers, and the longest baseline in the array. For completeness, we perform two sets of simulations, first with a 10° FWHM Gaussian beam, and then with a more realistic HERA beam derived from Fagnoni et al. (2021) simulations. The Gaussian beam is completely smooth while the HERA beam has realistic nulls and sidelobes. Since both `matvis` and `pyuvsim` use the `UVBeam` object from `pyuvdata` to handle beam evaluation and interpolation, this comparison provides good tests on how the beam structures influence `matvis`’s matrix-based RIME. Figure 1 shows the transit tracks of the 10 brightest sources in our sky model, overlaying on top of the zenith-pointed HERA beam amplitude (top), and the elevation angle of the sources as a function of LST. This information will become handy as we discuss our simulation results.

Figure 2 and 3 show visibility amplitude as a function of time from the simulations with Gaussian and HERA beams respectively. The top row in each of these two figures shows the results from `matvis` simulations, while the bottom row shows the percentage residuals

⁷ See https://pyuvsim.readthedocs.io/en/latest/parameter_files.html

⁸ <https://github.com/HERA-Team/matvis>

⁹ https://github.com/HERA-Team/hera_sim

¹⁰ <https://github.com/RadioAstronomySoftwareGroup/pyuvsim>

¹¹ <https://github.com/RadioAstronomySoftwareGroup/pyuvdata>

¹² http://reionization.org/wp-content/uploads/2013/03/HERA067_HERA_Software_Community_Guide_6May2019.pdf

¹³ <https://matvis.readthedocs.io>

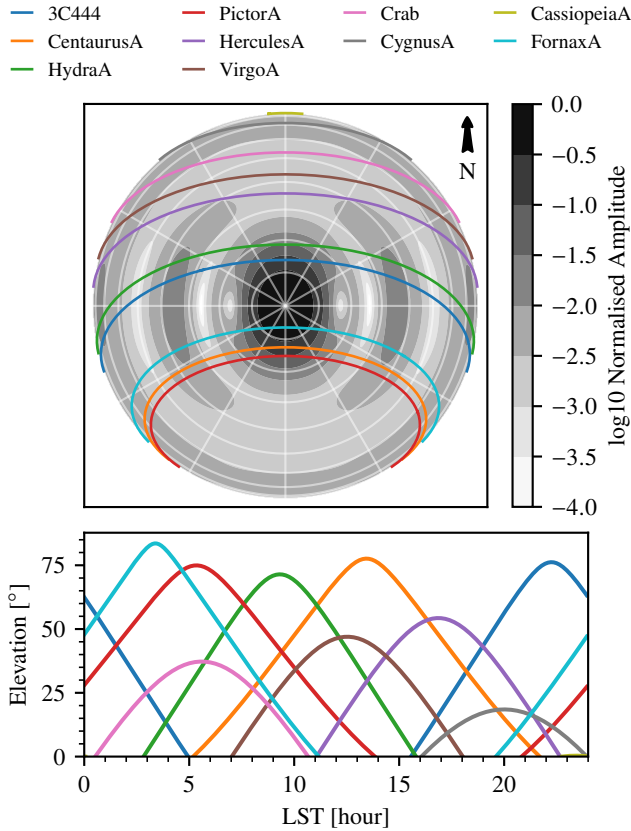


Figure 1. Tracks of the 10 brightest sources in our point-source model overlaying on top of the zenith-pointed HERA beam (top), and the elevation angle of the sources as a function of LST (bottom).

between `matvis` and `pyuvsim`,

$$|V|_{\text{residual}} = \left| \frac{V_{\text{pyuvsim}} - V_{\text{matvis}}}{V_{\text{pyuvsim}}} \right| \times 100\%. \quad (10)$$

The vertical dashed lines indicate the reference times for equatorial-to-horizontal coordinate transformation in `matvis`, which are set to 12 h for these simulations. Figure 4 shows the visibility phase residuals as a function of time between the two simulators, with the top and bottom rows showing results from simulations with Gaussian and HERA beams respectively. In all three figures, the left and right columns show results from E-W and N-S baselines.

First, we can see from the top panels of Figure 2 and 3 that `matvis` simulations follow the expected amplitude responses. The two strong peaks at ≈ 3 and ≈ 13 h correspond to Fornax A and Centaurus A, the two bright sources $\approx 7^\circ$ and $\approx 17^\circ$ away from the meridian, transiting across the telescope. We see very smooth responses at the shortest 14-m baselines and more oscillations as the baseline lengths increase due to the more rapidly oscillating fringe patterns. The differences between the Gaussian and HERA beam cases, e.g. between 12 – 24 h, are due to the sources interacting with the sidelobe responses of the HERA beam.

Looking at the amplitude residuals between `pyuvsim` and `matvis`, we can see clear effects from `matvis` equatorial-to-horizontal coordinate transformation scheme. The residuals reach the lowest level of $\approx 10^{-5}$ percent at LST = 12 h, which is the time used as the reference time for our coordinate transformation. The horizontal source positions are the most accurate at this time, resulting in less errors in the phase terms in Equation 4, and thus the most accurate simu-

lations. At other times, `matvis` results deviate more from `pyuvsim` due to source position errors, and hence more errors in the phase term, and less accurate simulations. We also see that the amplitude residuals are higher at longer baselines due to the finer fringe patterns requiring more accurate source positions. Effects of the source position errors can be seen more clearly in the visibility phase residuals in Figure 4. There is a clear trend of increasing residuals at times further away from the 12-h reference time. The residuals jump at ≈ 1 h, when bright sources, such as Fornax A and Pictor A, cross into the sidelobe of the telescope beam response, amplifying errors from the source position inaccuracy, although this is less problematic in N-S baselines because the sources move against the N-S orientation. Outside of these jumps the phase residuals are less than $\approx 0.5^\circ$. We will investigate the effects of `matvis` coordinate corrections in more detail later in the section.

One concern in 21 cm cosmology data analysis is structural smoothness in the Fourier domain. Specifically, a visibility simulator should not introduce temporal or spectral structure that would appear as systematics in the pipeline. Given that the phase term in the `matvis` RIME (Equation 5) is especially prone to errors in the time-dependent horizontal source positions, as we have shown in Figure 4, we expect some discrepancies in the temporal structures of the visibilities between `matvis` and `pyuvsim`. On the other hand, we expect spectral structure to be less problematic as frequency-dependent parameters, such as the beams and baseline vectors, mostly affect the scaling of the visibilities.

We validate the temporal structures in `matvis` simulations by Fourier transforming the output complex visibility used in Figure 2, 3, and 4 in time to the fringe-rate domain before calculating the amplitudes and phases and comparing with `pyuvsim`. A Blackman-Harris window function is applied to the data in the time dimension before the Fourier operation. Results are shown in Figures 5, 6, and Figure 7. We note that the fringe rate axes are cropped from the full range (-50 to 50 mHz) in these figures.

Overall, `matvis` simulations produce expected amplitude and phase responses over fringe rate and agree well with `pyuvsim`. The fringe rate is the rate at which the angular structure of the sky moves relative to the fringe pattern, which depends on the baseline vectors and positional vectors of the sources (Parsons et al. 2016). For a HERA-like, drift-scan, telescope that we have simulated, the projected path length difference (of the travelling radio waves) onto the N-S baselines does not change as a source moves from East to West. Thus, the amplitude responses over fringe rate from N-S baselines are centred near zero mHz as apparent in the top right panels of Figures 5 and 6. On the other hand, responses from E-W baselines peak at different fringe rates for different baseline lengths as shown in the top left columns of the figures. The residual amplitude levels over fringe rates are on average 1 and 0.1 percent or lower for simulations with Gaussian and HERA beams respectively, with no visible spurious temporal structures. The shorter baselines are in better agreement between the two simulators, showing lower levels of residuals for the same reason previously mentioned. One thing to note is the raised shoulder levels (outside of the peaks) in the simulations with HERA beams, which appear to be 3–5 orders of magnitude higher than in the simulations with Gaussian beams. These are sidelobe effects of the HERA beams, not an error in the simulations, and should not be concerning since both simulators agree well. The visibility phase residuals over fringe rate are in general near zero, with spurious jumps that can be as high as several tens of degrees. These jumps are exactly the same among multiple simulation runs of the same parameters, indicating that they are fixed to the sky models, beams, and other simulation parameters. The Gaussian beam produces more

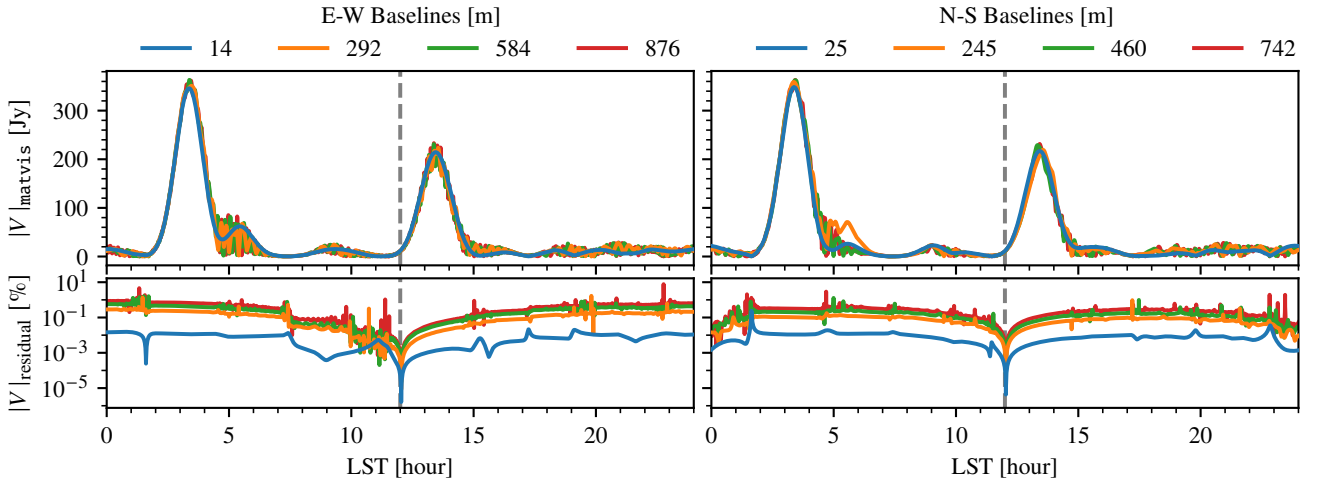


Figure 2. Visibility amplitude as a function of LST from `matvis` simulations with point-source sky models and 10° FWHM Gaussian beams (top) and residual against `pyuvsim` simulations with the same parameters (bottom). The left and right columns show results from E-W and N-S baselines. The vertical dashed line at LST = 12 h marks the reference time for `matvis` coordinate transformation.

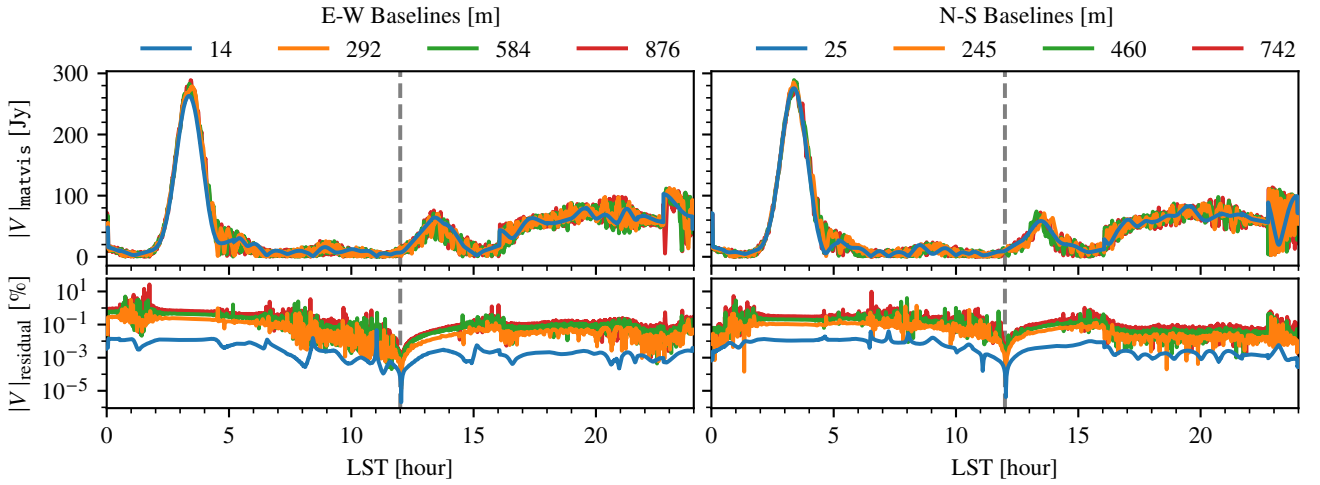


Figure 3. Same as Figure 2 except that results are derived from simulations with HERA beams (Fagnoni et al. 2021).

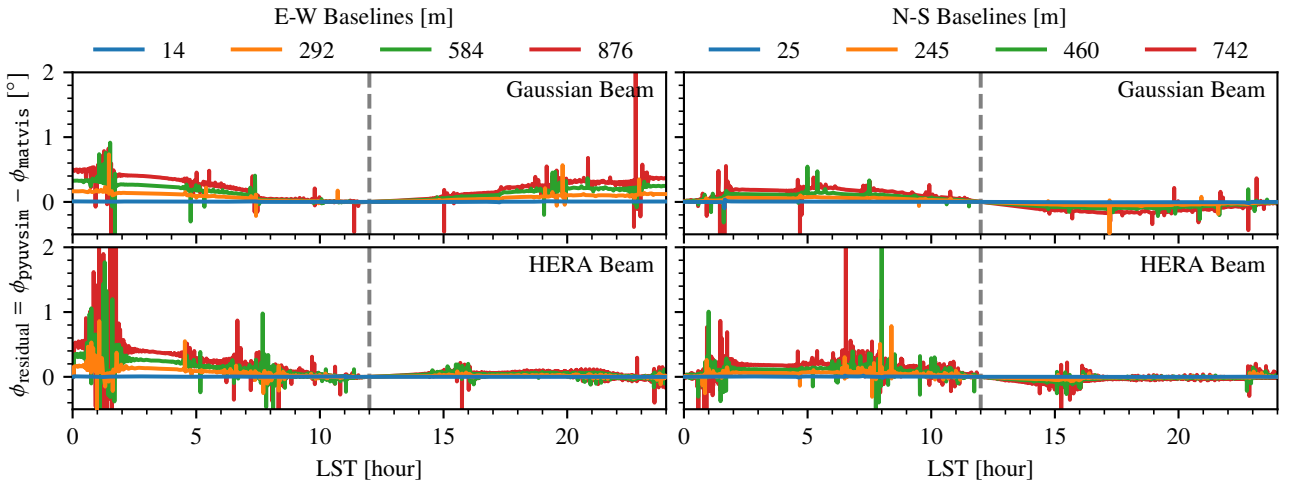


Figure 4. Visibility phase differences between `pyuvsim` and `matvis` point-source simulations as a function of time. The left and right columns correspond to E-W and N-S baselines, while the top and bottom rows correspond to simulations with Gaussian and HERA beams respectively. Vertical dashed lines at LST = 12 h indicates the reference times for `matvis` coordinate transformation. The accuracy of the source positions in `matvis` RIME decreases at times further away from the reference time, resulting in an increase in the phase residuals.

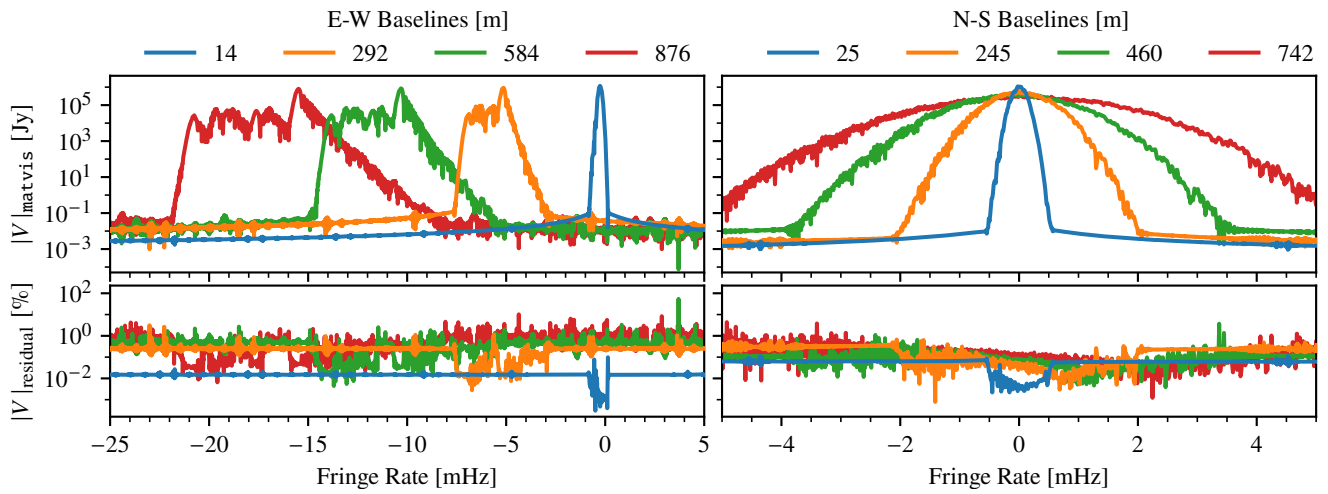


Figure 5. Visibility amplitude as a function of fringe rate from *matvis* point-source simulations with 10° FWHM Gaussian beams (top) and residual with *pyuvsim* (bottom). Arrangement and styling are the same as in Figure 2.

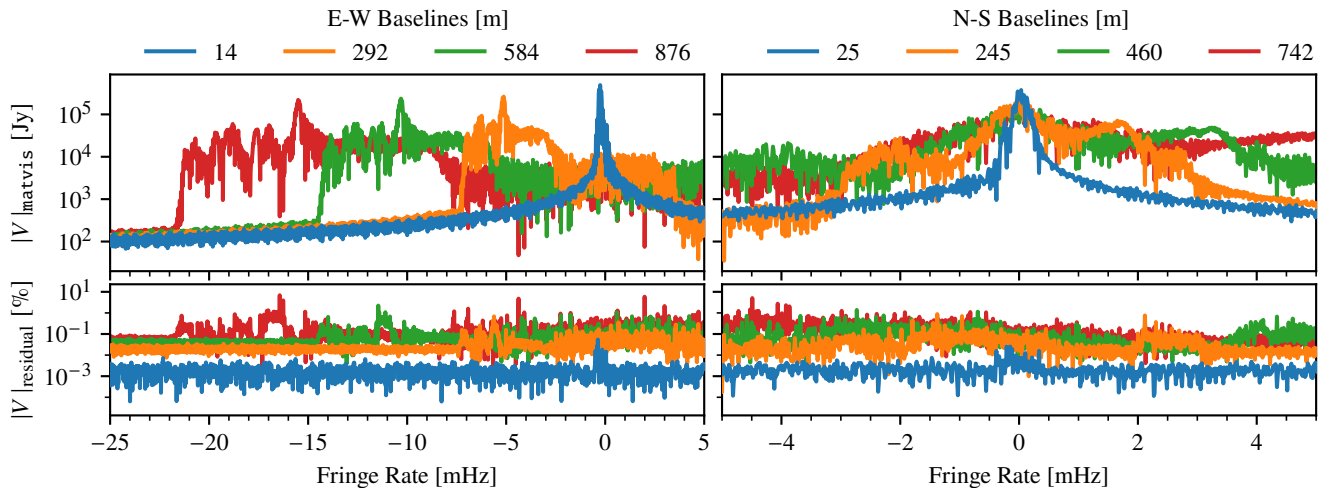


Figure 6. Same as Figure 5 except that the results are derived from simulation with HERA beams.

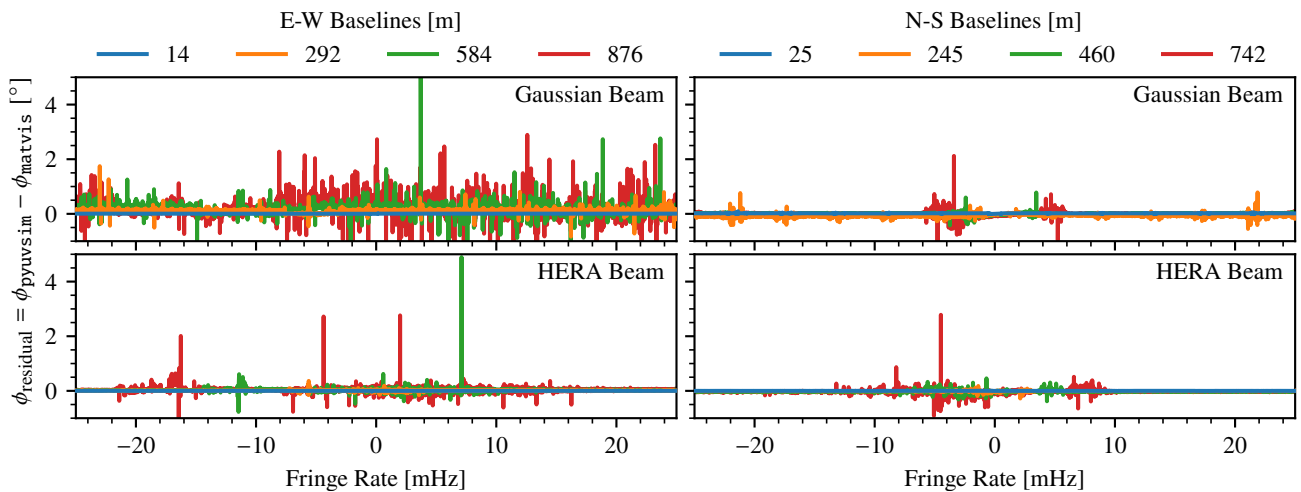


Figure 7. Visibility phase residuals between *pyuvsim* and *matvis* point-source simulations as a function of fringe rates. Organisation and marking are the same as Figure 4.

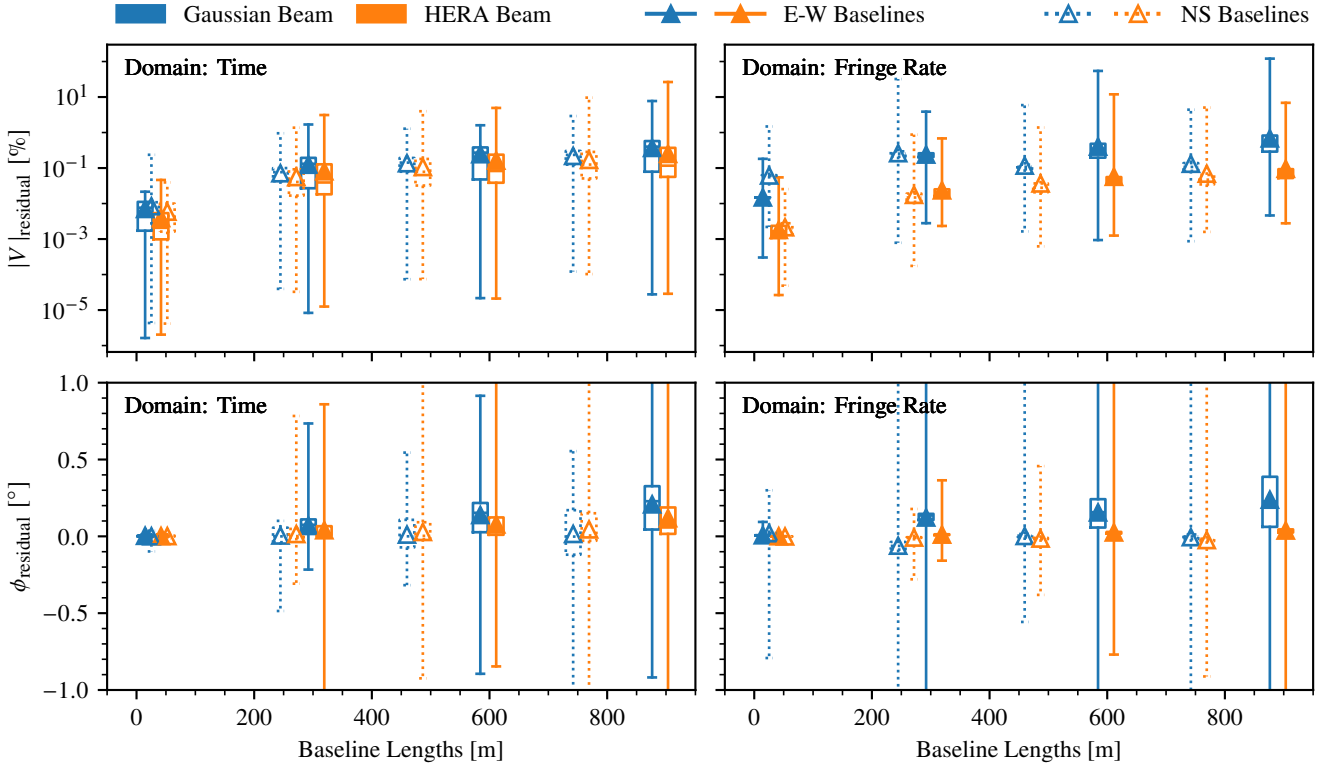


Figure 8. Statistics of amplitude and phase residuals between `matvis` and `pyuvsim`. Each box shows the IQR range (25th to 75th percentile) of the amplitude or phase residuals over time or fringe rate as annotated. The horizontal line in each box indicates the median while the triangle indicates the mean. The whisker shows the minimum to maximum range. For all cases, `matvis` agrees relatively well with `pyuvsim`.

of these spurious jumps in the phase residuals, especially in the E-W baselines. Combined with what we learned in the time domain (Figure 4), the bright source transiting the telescope and the less accurate source positions in `matvis` are likely responsible for the changes in the phase values relative to `pyuvsim`, resulting in jumps in these residuals.

To provide more quantitative assessment, we summarise statistics of the amplitude and phase residuals from the previous six figures in the box-and-whisker plot in Figure 8. Here, each box shows the interquartile range (IQR), the difference between the 75th and 25th percentiles of the residuals in LST or fringe rate at the indicated baseline. The horizontal line in the middle of the box shows the median while the triangle mark shows the mean. Unconventional to this type of plot, we show the full minimum to maximum range of the differences using the whiskers. In all cases, the IQR is less than ≈ 0.5 percent and $\approx 0.5^\circ$ for amplitude and phase residuals respectively, with very compact boxes around the means and medians. These suggest that `matvis` statistically agrees with `pyuvsim` although some spurious differences can occur, especially in the fringe rate domain. Whether or not these are good enough, once again, will depend on individual use cases.

To validate spectral structure, we simulate another set of visibilities at LST = 3, 14, and 20 hr over a 100–140 MHz frequency range using same point source catalogue and the HERA beam. We Fourier transform the complex visibilities along the frequency dimension into the delay domain with the Blackman-Harris taper before calculating the amplitude and phase residuals against `pyuvsim` as before in both frequency and delay domains. Figures 9 and 10 show results from these tests. As expected, the residuals are small but not zero in both frequency and delay, showing up to be under 10^{-5} percent

and 10^{-6} degree for amplitude and phase. The residuals are mostly linear with positive slopes in frequency (as opposed to the expected flat residual responses). These slopes are steeper for longer baselines and are more obvious in the phase. They may also be products of source position errors in `matvis` as higher frequencies have better angular resolutions and are thus more sensitive to the fact that the sources are at slightly different positions. Since these are linear and the overall residual levels are small, they are not particularly concerning for HERA pipeline validation. The more concerning features are the strong fluctuations in certain LSTs, e.g. 14 h, that clearly deviate from the positive-slope trend, and become stronger and oscillate more rapidly for longer baselines, suggesting that bright sources transiting across the sidelobes of the HERA beams are the sources of these fluctuations. In the case of LST = 14 h, this source is Centaurus A. We confirm this by re-running the simulations with Gaussian beams, which have no sidelobes, and the residual responses become completely smooth. Small-scale fluctuations are also present overlaying on top of the overall responses. These are likely caused by numerical errors considering their noise-like oscillation and very low levels. It is also interesting to note that the phase residual over frequency is positive for E-W baselines and negative for N-S baselines.

4.1.1 Effects of `matvis` coordinate transformation

As discussed, the way that coordinate corrections are set up in `matvis` can greatly influence the accuracy of the results because the source position errors strongly affect the phase term. This effect is especially clear in the amplitude of phase residuals over time (Figure 2–4), where the residuals are lowest at the reference time and increase as the time separation increases from the reference. We have

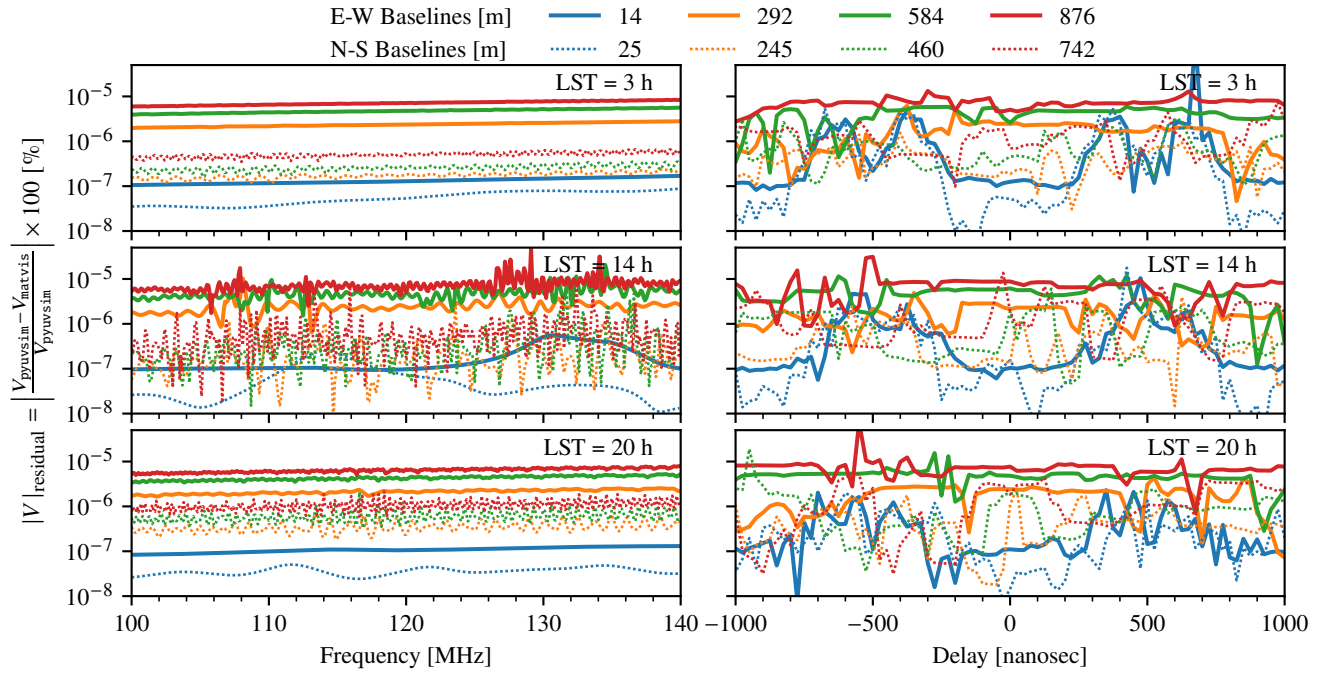


Figure 9. *matvis* amplitude residuals against *pyuvsim* in frequency and delay (Fourier transform of frequency) at selected LSTs. *matvis* agrees relatively well with *pyuvsim*. The residuals exhibits slight positive slopes in frequency. Strong fluctuations at LST = 14 h are due to Centaurus A transiting across the sidelobe of the HERA beam. Small fluctuations are likely numerical errors based on their levels. These fluctuations propagate to structures in the delay domain.

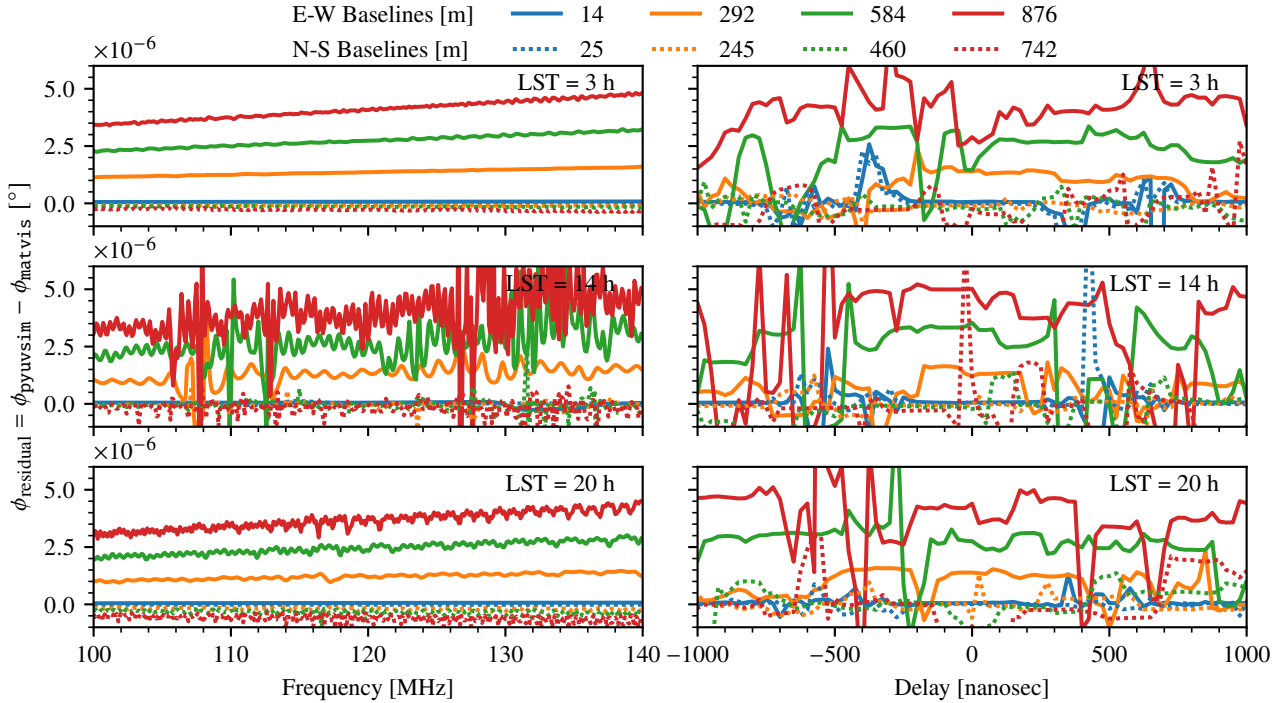


Figure 10. *matvis* phase residuals against *pyuvsim* in frequency and delay at selected LSTs. The phase residuals exhibit similar behaviours as the amplitude residuals in Figure 9 although the positive slopes in frequency is more clear.

also demonstrated that bright sources transiting the sidelobes of the telescope primary beams can amplify this error. This is especially clear in Figure 4 at around 1.5 h when Fornax A is starting to come into the view of the telescope.

We can take advantage of these behaviours to improve the ac-

curacy, i.e. reduce the residual between *matvis* and *pyuvsim* by changing the reference time or splitting the simulations into multiple time chunks, each of which uses its own local “reference time”. To demonstrate, we rerun *matvis* simulations used in Figure 2–4 by: (a) using the time where Fornax A is at zenith as the reference

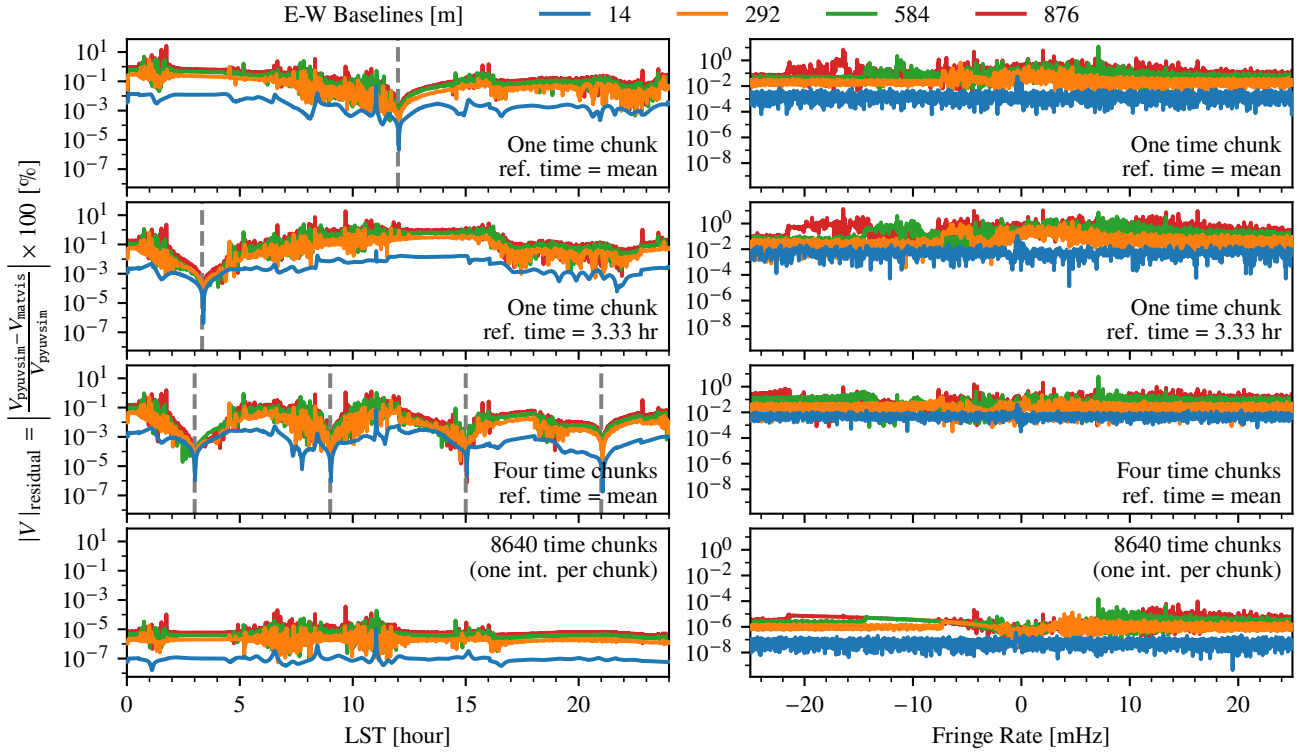


Figure 11. Demonstrating effect of source positions errors in *matvis* coordinate transformation scheme. The left and right columns show the visibility amplitude residuals from simulations with the HERA beam as a function of time and fringe rate. Each panel correspond to different simulation scenarios and different reference times used for source position correction as annotated. By changing the reference times used in the source position corrections and splitting the simulation into multiple time chunks, errors in the visibilities due to source position errors can be minimised.

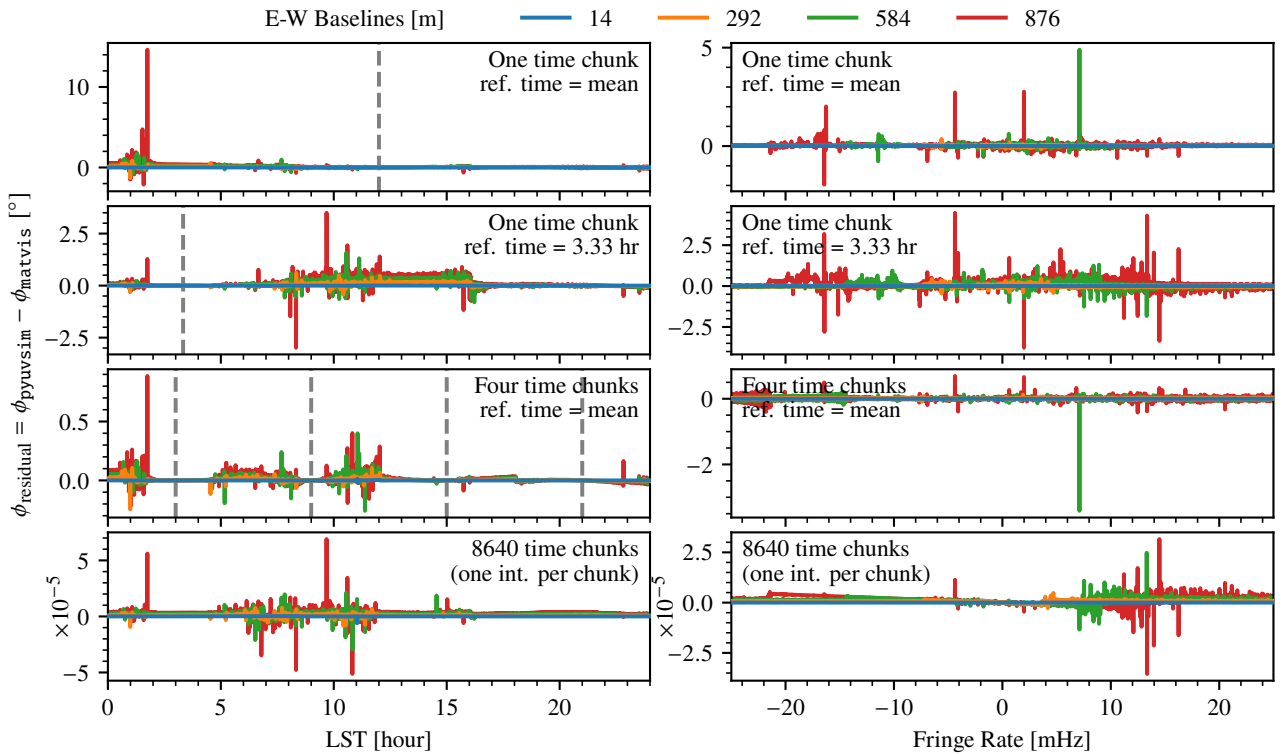


Figure 12. Same as Figure 11 but plotting the visibility phase.

time for `matvis`'s coordinate transformation, (b) splitting the 24-h simulations into 4 chunks, and (c) splitting into 8640 chunks, i.e. every time-step being referenced exactly to the `astropy` coordinates of itself. Among these, (c) will be the most accurate. The results are shown in Figure 11 and 12.

Comparing with the original simulations that use LST = 12 h as reference times (top rows), we can clearly see that setting the reference time to the Fornax A's position (second rows from the top) can significantly reduce the amplitude residuals and the jump in the phase residuals around 3 h. However, by doing so, the residuals have increased at 12 h. Splitting the simulation into four chunks (third rows), each chunk simulating 6 h and using the mean time as a reference time, can further improve the residuals although the residuals are still lowest at the reference times and increase further away. By simulating 1 time step at a time (bottom rows), we can clearly see the residuals are minimised. This is, however, not an effective way of running `matvis` due to overhead cost. Splitting the simulations into 2+ time chunks can still significantly benefit the accuracy of the simulations. Specifically, the source position errors are at maximum at ≈ 6 h from the reference time. Then, it will reduce to reach the minimum again at ≈ 24 h from the reference time, and the cycle repeats. This is because the corrections that `matvis` uses are tied to the equatorial coordinates of the sources; thus, the sources will appear at the horizontal coordinates corresponding to the chosen reference times again every slightly less than 24 h. Choosing the size of the time-chunks appropriately will depend on the use-case; overheads associated with multiple chunks can become negligible when the number of antennas is large.

4.2 Diffuse Simulation

As discussed extensively already, `matvis` assumes the point-source approximation for the sky model. To simulate visibilities from a resolved radio galaxy with extended jets or diffuse emission, the user must first discretise the sky intensity into a set of delta functions that are assigned the integrated flux of surrounding regions. `matvis` is agnostic to the specific choice of this pixelisation, e.g. the position of each pixel, except that it gives equal weight to each pixel, although each pixel does not need to occupy equal surface area on the sky. In other words, it is either that each pixel occupies an equal area, or that fluxes from all pixels sum up to the total integrated flux density from the sky. For diffuse emission, one choice of explicit pixelisation that is consistent with these assumptions is the HEALPix pixelisation. However, the calculation of the RIME is expected to break down on long baselines for HEALPix maps with coarse pixels that do not sufficiently sample the fringe patterns.

To demonstrate, we simulate visibilities from the Global Sky Model (GSM; de Oliveira-Costa et al. 2010) at several different HEALPix resolutions with `matvis` and compare the outputs. We use the `pygsm` package (Price 2016) to generate the GSM maps. The natural resolution of these maps, defined by its `NSIDE` parameter, is 512, corresponding to a pixel resolution of 6.87 arcmin. We first smooth this map with a 1° FWHM Gaussian kernel and then downgrade, using the `udgrade` function of the `healpy` package (Zonca et al. 2019), to `NSIDE`=256, 128, and 64, corresponding to pixel resolutions of 13.74, 27.48, and 54.96 arcmin respectively. The Gaussian smoothing ensures that the sky information in the maps is well enough sampled by all of our chosen HEALPix resolutions. We simulate a zenith-pointing drift-scan observation over 1 h of LST with 5 s of integration (JD 2458208.9162 to 2458208.9595) at 250 MHz with the HERA telescope configuration and beam (same as in Section 4.1) for E-W baselines of 14, 102, and 219 m. Source posi-

tion correction described in Section 2.3 is applied, using the mean of observation time as a reference time. Figure 13 and 14 shows the amplitude and phase of the `matvis` visibilities as a function of LST (left columns) and fringe rate (right column). Blackman-Harris taper function is used when calculating the fringe rate visibility as before. Each row corresponds to a different baseline length, and each line in each panel corresponds to a different HEALPix resolution as indicated.

First, we note that the cases with `NSIDE`=512 will produce the most accurate results because the fringes are very well sampled at this resolution. For the 14-m baselines (top rows), the fringe spacing is $\approx 5^\circ$, which is coarse enough to be well sampled by all HEALPix resolutions in our test cases, resulting in no aliasing, yielding visibilities that have the same smoothly varying amplitude and phase responses across the LST for all HEALPix map resolutions. Moving to the 102-m baselines (middle rows), we see that the output from a map with `NSIDE`=64 resolution is completely off from the rest. The fringe spacing of a 102-m baseline at 250 MHz is ≈ 42 arcmin, which is finer than the 54.96-arcmin resolution of the `NSIDE`=64 map. This causes aliasing in both the amplitude and phase of visibilities as apparent in the figures. Looking at an even longer baseline of 219 m (bottom rows), we see a similar behaviour, in which the output from sky maps with `NSIDE`=64 and 128 deviate from the rest of the simulations for the same reason.

In the fringe-rate domain, we see an interesting effect, in which aliasing reduces dynamic range of the visibility amplitude. This appears as raised 'shoulders' of the amplitude–fringe-rate response (in comparison to the `NSIDE`=512 case) as demonstrated in the right column of Figure 13. High time-varying components of the visibilities correspond to the high (positive and negative) fringe rates, and aliasing due to insufficient sampling of the fringe patterns in low-resolution HEALPix maps will cause excess power in the high fringe-rate components. Longer baselines are especially prone to this effect, but it is also visible at the short 14-m baselines on lower map resolutions despite these maps having theoretically sufficient fringe sampling factors (e.g. factors of 5 and 10 for `NSIDE`=64 and 128). Looking at the phase over fringe rates on the right column of Figure 14, we see that the phases are well matched between -1 to 1 mHz at all baseline lengths and map resolutions, except for `NSIDE`=64 at 219 m. However, aliasing effects become apparent at the higher fringe rates, at which the phases are very much mismatched.

Based on our small set of tests here, it is difficult to deduce the 'rule-of-thumb' resolutions of diffuse sky models when simulating with `matvis` (or `pyuvsim`). The best resolution to use depends on a few factors: the nature of the sky models, baselines, and analysis requirement (i.e. time vs fringe-rate space). Certainly, finer pixelisation of the sky will produce more accurate results at a cost of computing time. We suggest that users conduct a small set of test runs, which should take a minimal amount of time given the speed of `matvis`, to determine the appropriate parameter choices for their simulation requirements. For detailed tests, analytical solutions to the full-sky diffuse emission presented in Lanman et al. (2022) should also be considered. It is also important to note that the issue that we have just demonstrated is intrinsic to the pixelisation of the diffuse sky and is not `matvis`-specific. Other simulators that use the point-source approximation, including `pyuvsim`, will encounter the same issue.

Nevertheless, `matvis` is still capable of producing simulations from diffuse sky components that are in good agreement with `pyuvsim`. We show this in Figure 15. Here, we run `pyuvsim` simulations with the `NSIDE`=128 diffuse sky map, dropping the 219-m baseline as we will not be able to produce the correct visibilities with this map resolution as demonstrated above. Then, we calcu-

late and plot the amplitude and phase residuals between `matvis` and `pyuvsim` simulations, as defined in Section 4.1. As apparent in the figure, `matvis` produces simulations that are in good agreement with `pyuvsim`. In the time domain, the residuals are mostly below 10^{-3} percent in amplitude and near zero in the phase. The maximum phase residual is less than 0.5° . In the fringe rate domain, the amplitude responses are in relatively good agreement although the phase responses suffered from source position errors at high fringe rates. These results should come as no surprise because the diffuse simulations are fundamentally the same as the point source simulations that we have already validated in Section 4.1 – the simulators are still operating on ‘point sources’ regardless of intrinsic nature of the input sky model.

5 COMPUTATIONAL PERFORMANCE AND OPTIMISATION

An important feature of `matvis` is its computational performance. Indeed, the consideration of performance is the driving motivation behind the matrix-based algorithm presented in Section 2.5, and the structuring of the Python implementation in a way that GPUs can be used as a drop-in replacement for CPUs. In this section, we will look at the relative contribution to overall run-time from each of the algorithm steps, determining the bottleneck(s). We will also explore how this run-time scales with different simulation parameters, numbers of cores, and how much acceleration is afforded by the GPU. We will also consider the memory footprint of the algorithm and associated concerns, and finally we will take a deeper look at the largest bottleneck—the matrix-matrix multiplication of step (v)—considering its theoretical complexity and potential optimisations.

5.1 Runtime Performance

Figure 16 summarises the runtime performance of `matvis`. Specifically, it shows the timing of a number of simulations with different numbers of source N_{sources} , antennas N_{antennas} , and times/snapshots N_{times} , using the script `matvis profile` included in the package. The script generates simulation configurations that take advantage of the fact that the performance cannot depend on the properties or locations of sources, the locations of antennas, or the precise frequencies or times of observation: only their total number. In addition to these dimensions, the performance will depend on the number of unique beams, N_{beams} , and whether they are analytic or simulated (and if simulated, the size of the grid onto which they are simulated), as well as the number of feeds per antenna, N_{feed} and whether the beams are E -field beams or not.

In Figure 16 we consider only the case where $N_{\text{beams}} = 1$, i.e. all antennas have the same beam (which is a common assumption). This beam is a complex-valued E -field beam evaluated on a 1-degree regular mesh for two feeds. To be representative of common simulation setups, the sources are distributed uniformly across the sky, which means that at any particular integration, half of them are below the horizon. In the current implementation of `matvis`, these sources are ignored (for that given integration), which potentially impacts performance.

Figure 16 shows the impact of three parameters. Our ‘default’ value for each is $N_{\text{sources}} = 2^{19} \approx 525\text{k}$, $N_{\text{antennas}} = 256$ and $N_{\text{times}} = 16$. Keeping two parameters fixed at their default, we run the third parameter over a logarithmic grid: $N_{\text{sources}} \in 2^{\{10, \dots, 19\}}$, $N_{\text{antennas}} \in 2^{\{3, \dots, 8\}}$ and $N_{\text{times}} \in 2^{\{0, \dots, 7\}}$. Run-times are shown for the CPU (orange) and GPU (blue), with the default run shown in

black. We also show the run-time for the default set using `pyuvsim` as a black square. Different marker symbols indicate steps of the algorithm (cf. Section 2.5), which we will discuss in more detail momentarily. These profiling simulations were performed on the Ilifu cloud-computing cluster¹⁴ in Cape Town, South Africa. The CPU profiles are computed on a 2.6GHz Xeon Processor using a single core for each run. The GPU profiles are computed on NVIDIA V100 GPU. Note that the results shown are for a single frequency; there is almost perfect pluralisation between frequencies, and virtually no overhead from computing a single frequency in a single job. There are two caveats to this: firstly, the computation of the array \mathbf{R} for all time-steps can be done once for all frequencies, and secondly, writing out the simulated data to disk can be more efficient when frequencies are grouped together. The computation of \mathbf{R} is included in the total time shown in Figure 16, contributing to the small overhead. I/O overheads from reading the beam are included, but not from writing the results to disk. The total run-time (for both CPU and GPU) is calculated by simply measuring the wall-time of the entire calculation. The run-time of individual algorithm steps is measured on the CPU by using the `line_profiler` Python package. On the GPU, since each step corresponds to a particular CUDA kernel, we use the `nvprof` utility which specifically measures performance of kernels at runtime. We note that the sum of the run-times of individual steps should be strictly *less* than the total time, which also takes into account overheads outside the main loop of the algorithm as well as internal overheads (e.g. Python for-loop overhead).

The first thing we notice is that the scaling with N_{times} is almost perfectly linear for all steps of the calculation. This is exactly as we expect, since each step is run once per loop and the overhead outside the loop is very minimal compared to the run-time of the default parameters. The scaling with N_{antennas} and N_{sources} is far more interesting, and varies amongst the different algorithm steps.

A second obvious takeaway is that the GPU accelerates the computation by a factor of ~ 100 for the larger simulations tested here. This is clearly dependent on the properties of both the CPU and GPU used, but should be a good rule-of-thumb. Even the slower CPU implementation is $\sim 40\times$ faster than the `pyuvsim` simulator in its current form.

For both GPU and CPU, the major component in terms of run-time is the matrix-matrix multiplication, step (v). For the majority of problem sizes on the GPU, this step is a factor of ~ 5 more expensive than the next-most-expensive step, which is generally the calculation of the per-antenna matrix \mathbf{Z} , i.e. step (iv). Interestingly, on the CPU this is only true for the largest N_{antennas} considered here: for smaller N_{antennas} , step (iv) is dominant. The scaling of these two steps with N_{antennas} is expected to be different, with step (v) naively scaling more strongly than step (iv), which explains this cross-over for large N_{antennas} . Another caveat to this picture is that on the GPU, when $N_{\text{sources}} \lesssim 10^5$ or $N_{\text{antennas}} \lesssim 128$, the dominant contribution to run-time is in fact *overheads*, which for this setup appear to be about one second. While some of this overhead is from outside the time-loop, inspection of the profile reveals that much of the overhead is from within the time-loop (between GPU operations), and therefore will scale with N_{times} . This will present an issue for simulations with small N_{ant} with large N_{times} , but can perhaps be overcome with further optimisations to the Python code. A final caveat is that while the beam interpolation is a negligible component here, this is partially because we have used $N_{\text{beam}} = 1$, whereas in principle it could scale with N_{antennas} if all antennas are simulated with varying

¹⁴ <https://www.ilifu.ac.za/>

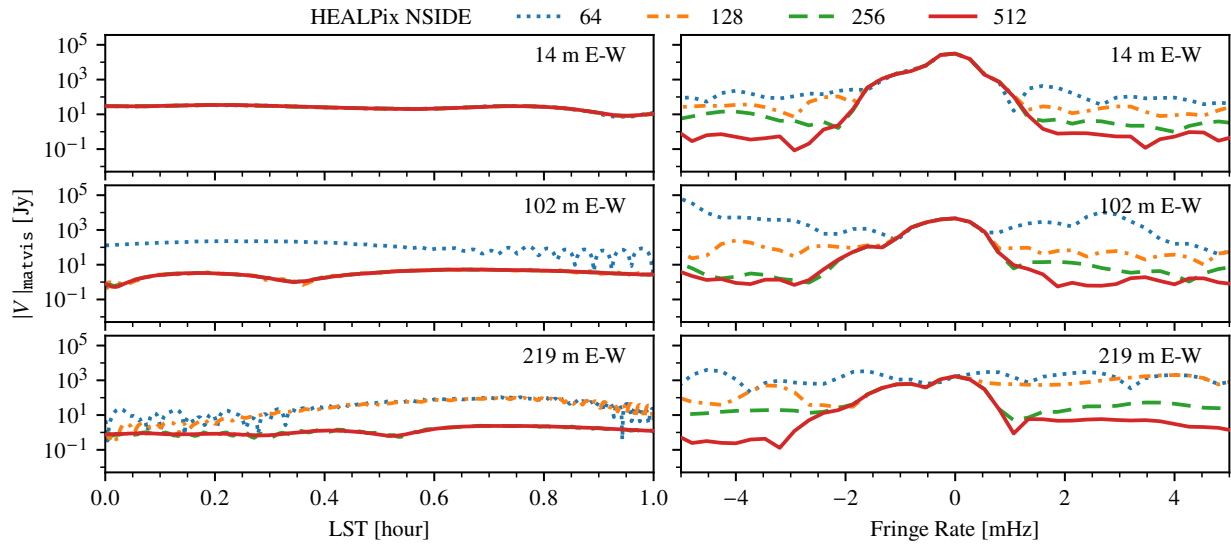


Figure 13. Demonstrating effects of pixelised diffuse sky model on *matvis* visibilities. The visibility amplitude from simulations with pixelised diffuse GSM models on various resolution HEALPix grids are plotted over time and fringe rate. Notice that simulating a longer baselines from the model with a coarse HEALPix resolution can result in aliasing, e.g. at 102 m E-W baseline with NSIDE=64 sky model. This behaviour is intrinsic to all simulators that use pixelised sky.

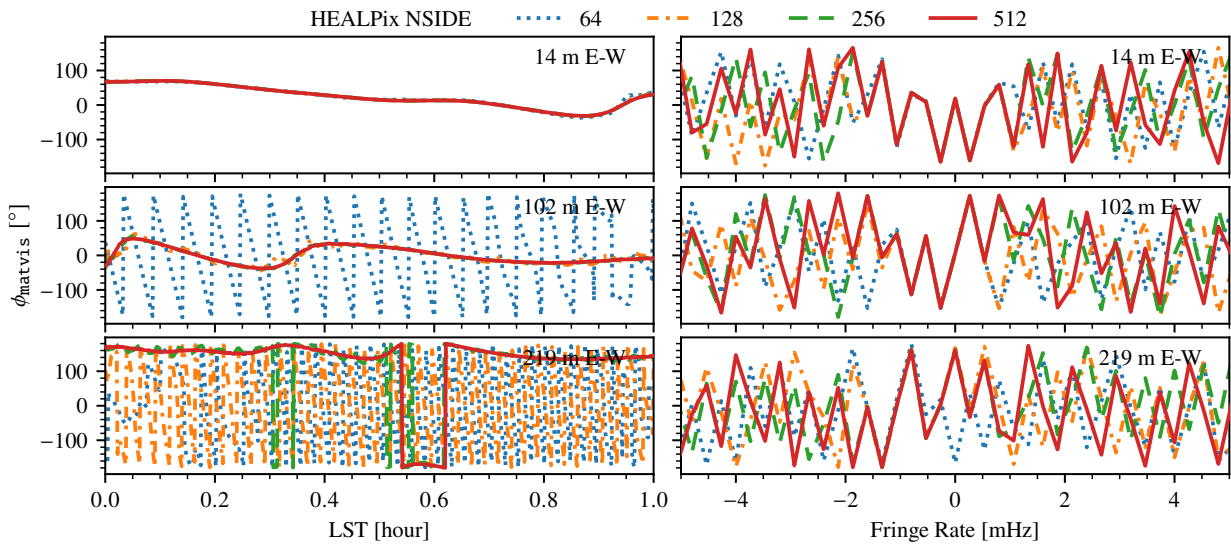


Figure 14. Same as Figure 13 but plotting the visibility phase.

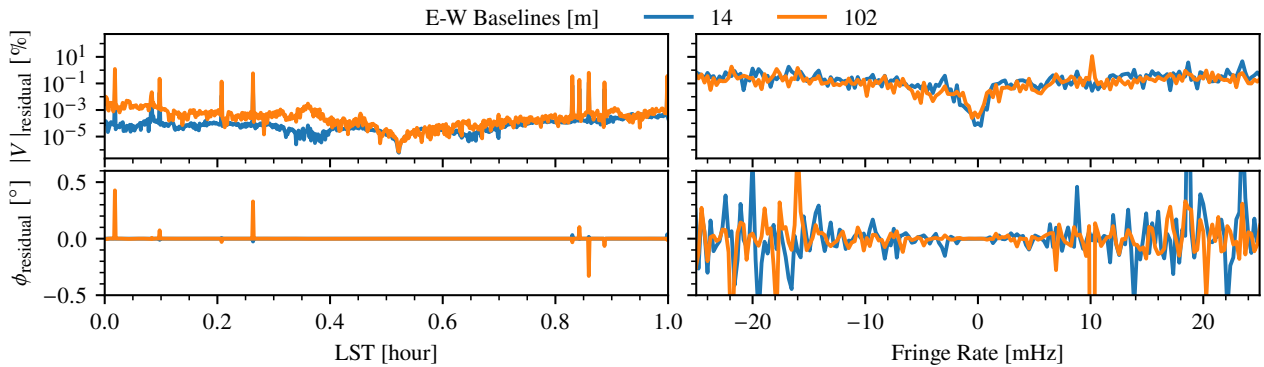


Figure 15. *matvis* visibility amplitude and phase residuals against *pyuvsim* when simulating from pixelised GSM model on a HEALPix grid. *matvis* still produce simulations that are as accurate as *pyuvsim* as expected.

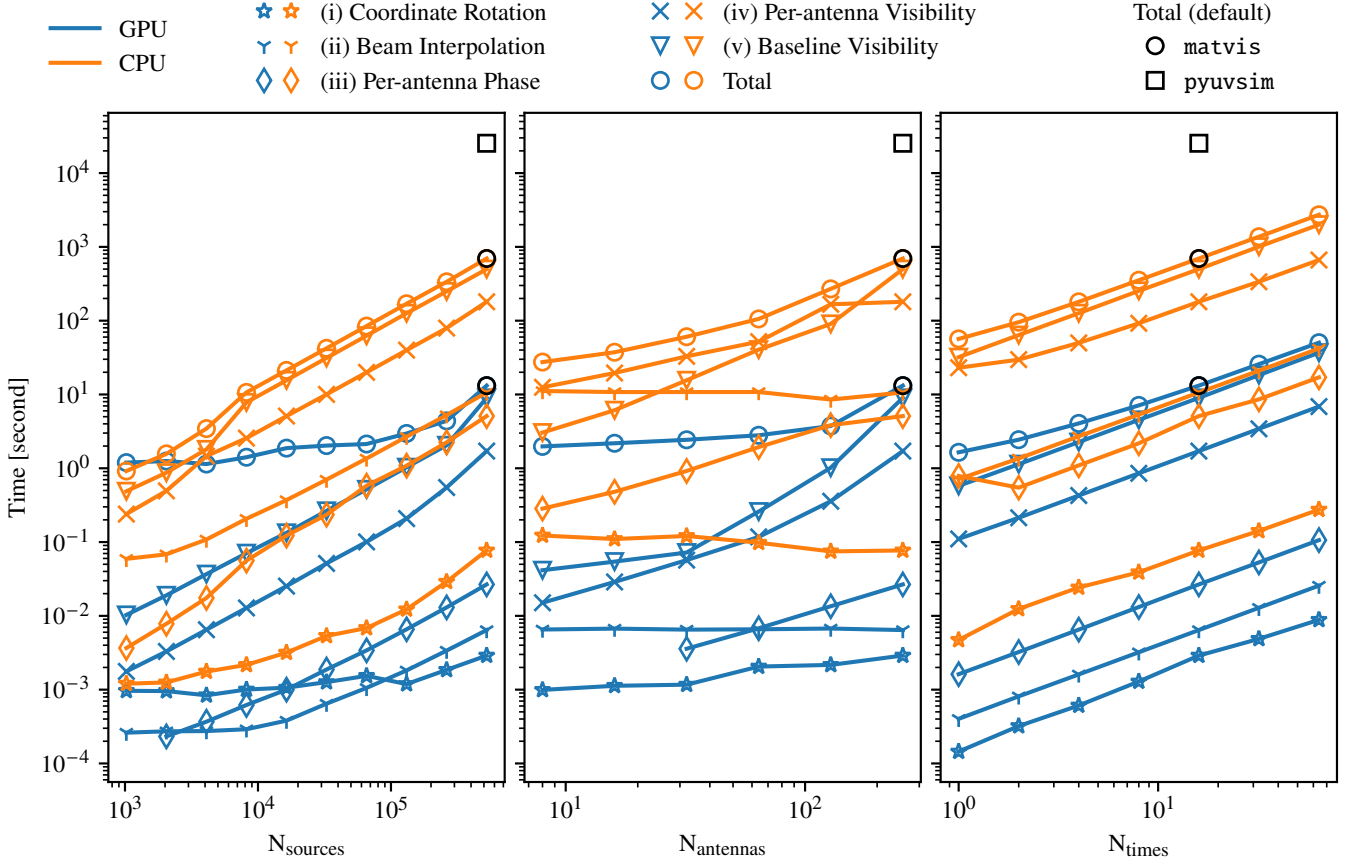


Figure 16. Scaling test results of the CPU and GPU implementation of `matvis`. Orange and blue colours indicate CPU and GPU results, while the different markers indicate steps in the calculation as described in Section 2.5. The wall time for the default simulation parameters ($N_{\text{antennas}} = 256$, $N_{\text{sources}} = 2^{19}$, $N_{\text{times}} = 16$) are shown in a black circle markers for `matvis` and a black square marker for `pyuvsim` for comparison.

beams. If this is the case, it would become the *dominant* step on the CPU up to very large N_{antennas} (where step (v) would overtake due to its hyperlinear scaling), and on the GPU it would be similar to step (iv) in its impact.

5.2 Multi-Cores CPU Performance

Modern linear algebra and interpolation routines, such as those in NumPy and SciPy, can take advantage of multiple CPU cores through multi-threading. To measure this performance, we run the profiling script with the default parameter set giving 2, 4, 8, 16 and 32 number of CPUs per job. We compile NumPy with the Intel Math Kernel Library, and set the `MKL_NUM_THREADS` environment variable to the number of CPUs used in each job to specify the number of threads. Figure 17 shows the scaling test results. Different markers correspond to different steps in `matvis` as in Figure 16. The grey dashed line indicate linear scaling (i.e. -1 slop). Notice that only step (v), which forms the per-baseline visibilities through the matrix product of the per-antenna visibilities, benefits from multi-threading. The scaling is linear until ≈ 4 CPUs, and then it flatten off. While further CPU cores do continue to speed up step (v), step (iv) becomes the bottleneck by that point since it is simply performing complex array arithmetic, and it does not benefit from multi-threading. Thus, we recommend that each job is given 2-4 cores when simulating with the CPU implementation.

5.3 Optimisation

Given the above observations, the crucial components to optimise for the majority of current use-cases are steps (iv) and (v) – and particularly (v) as the number of antennas grow larger in modern experiments (for example, SKA Phase II will have 512 antennas, double the maximum tested in this section).

Step (iv) naively has complexity $O(N_{\text{ant}}N_{\text{src}})$, and this is borne out in Figure 16 and 17. It requires calculation of a complex-exponential for each of the terms, which can be quite computationally expensive. However, it is also naively parallelism over either the source or antenna axes. Which is more convenient depends on the memory layout of the input and output arrays.

Step (v) is a more interesting problem. Naively, its complexity is $O(N_{\text{ant}}^2N_{\text{src}})$. This scaling applies inescapably to traditional simulators that compute the RIME as a set of N_{baseline} tasks, of each which computes Equation 3, since $N_{\text{baseline}} \propto N_{\text{ant}}^2$. However, our matrix-based approach makes use of highly-optimised algorithms for one of the most common operations in all computing: the matrix-matrix product. The matrix \mathbf{Z} has shape $N \times M$, where $N = N_{\text{ant}}N_{\text{feed}} \sim 10^{2-3}$ and $M = N_{\text{ax}}N_{\text{src}} \sim 10^{5-6}$. For *square* matrix multiplication ($M \equiv N$), the optimal complexity is known to be $O(N^\omega)$, with $\omega \approx 2.37$ or better (Vassilevska Williams et al. 2023). For more generic rectangular matrix multiplication, Le Gall & Urrutia (2017) places $\omega(k) < 2 + k$ as an upper bound for multiplying an $N \times N^k$ matrix by an $N^k \times N$ matrix for $k \leq 5$ (e.g.

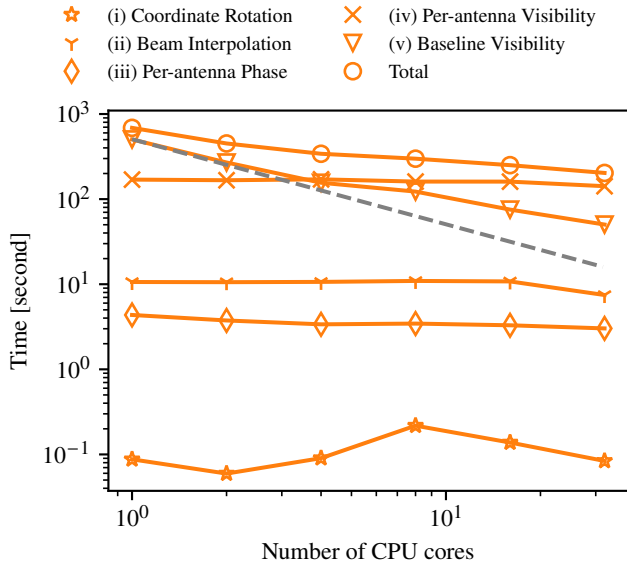


Figure 17. Scaling test results for multi-cores CPU performance of `matvis`. The grey dashed line indicates a linear scaling.

$\omega \leq 6.16$ for $k = 5$). Thus, an optimised matrix multiplication algorithm should perform better than $\mathcal{O}(N_{\text{ant}}^2)$ even in the realistic situation where $N_{\text{src}} \gg N_{\text{ant}}$. We have checked several commonly-used Python routines, and found the complexities in the range of $\mathcal{O}(N_{\text{ant}}^{1.3-2})$, reaffirming this claim. Thus, the algorithm presented here has every chance of being unbeatable for simulating current and future large- N_{ant} experiments.

In detail, some choices need to be made about the implementation of the matrix-matrix product. For both the CPU and GPU the current implementation uses the ZGEMM routine from BLAS to perform the multiplication. Specifically, on the CPU, the call is made via the `numpy.dot` function, which internally uses a backend implementation of BLAS that is configurable by the user. In Figure 16 and 17, we used the MKL backend. On the GPU, we use the CuBLAS implementation. Comparison to other implementations (e.g. `ArrayFire`¹⁵ and `Magma`¹⁶) is ongoing.

Besides the choice of implementation package, there are further optimisations worth considering. For example, the product $\mathbf{V} = \mathbf{Z}\mathbf{Z}^\dagger$ contains hermitian symmetry that in principle can be exploited by the ZHERK routine in BLAS, reducing the computations by a factor of two. However, we have found this approach to be less performant than the full ZGEMM for a range of realistic problem sizes. This is most likely due to the highly-irregular size of the matrices involved (i.e. $M \gg N$).

Another set of symmetries that this approach does not exploit are *baseline redundancies*: two baselines: ij and kl have equal visibilities if their beams are the same ($A_i \equiv A_k$ and $A_j \equiv A_l$) and their baseline vector is the same: $\mathbf{b}_{ij} = \mathbf{b}_{kl}$, regardless of the absolute positions of the antennas. For compact arrays like HERA—under the common assumption of ideal beams—the fraction of baselines which are redundant is very large ($\geq 95\%$), which means that ZGEMM is naively performing a factor of > 20 – 40 more calculations than necessary. We consider this problem in a little more detail in Appendix A, noting here only that for very large N_{ants} , the optimal scaling

of the matrix-multiplication will still win, even with the redundant calculations.

5.4 Memory Considerations

The way that the `matvis` algorithm is structured means that all steps inside the algorithm loop need only be stored in memory for a single snapshot, and only the final result needs to be kept for all snapshots. This final output is a complex array of size $N_{\text{ant}}^2 N_{\text{feed}}^2 N_{\text{time}}$. For the common case of $N_{\text{feed}} = 2$ and double-precision calculations, this is an array of size

$$\text{size}(\mathbf{V}) \approx \left(\frac{N_{\text{ant}}}{128}\right)^2 \frac{N_{\text{time}}}{1000} \text{ GB}. \quad (11)$$

Inside the loop, the largest array is \mathbf{Z} , with

$$\text{size}(\mathbf{Z}) \approx \frac{N_{\text{ant}}}{128} \frac{N_{\text{src}}}{130,000} \text{ GB}. \quad (12)$$

For the GPU implementation, this latter size is very important, as it is the dominant source of device-based memory. If N_{src} is very large, the peak memory (and device memory) can be easily reduced by splitting the sources into chunks, for minimal overhead (since the matrix-matrix calculation scales linearly with N_{src}), and `matvis` does this automatically.

Likewise, the total peak memory can be controlled by chunking the number of times, which incurs minimal overhead (according to Figure 16) as long as N_{ant} and N_{src} are reasonably large.

6 CONCLUSIONS

In this paper, we introduced a matrix-based optimisation of the RIME for simulating visibility from many-element radio interferometer as implemented in the `matvis` package. By first calculating per-antenna responses and then expanding them to visibilities through a simple outer product, `matvis` is able to utilise highly-efficient matrix operations, especially those implemented in GPU, to accelerate the calculation of the RIME. The algorithms assume a point-source approximation for the sky model, treating each of the components in the model as an unresolved point source with a defined total flux at a given frequency. To simulate from diffuse emission or extended sources, they must first be pixelised as an ensemble of point sources. To improve accuracy, which is sensitive to errors in the equatorial-to-horizontal coordinate transformation of the source positions, we introduce a computational trick that combines accurate astropy-based transformation with a fast rotational matrix-based conversion.

We validated `matvis`'s simulations against `pyuvsim`, a reference simulator that prioritises accuracy over speed. We performed two sets of validation tests, one with point-source sky models and another with pixelised diffuse sky models on HEALPix maps. For point-source simulations, we compared the amplitude and phase of the output visibilities from the two simulators in time, fringe-rate, frequency and delay domains. Our results show that `matvis` simulations agree relatively well with `pyuvsim` in most cases. However, bright sources interacting with sidelobes of the telescope primary beams, combined with the less accurate source positions that `matvis` uses, can cause the simulation to deviate from `pyuvsim`, appearing as jumps in the amplitude and phase residuals. This can be alleviated by setting the reference time for the `matvis` coordinate transformation to the transit time of the brightest source, and splitting the simulations into multiple (locally-referenced) time chunks as we have explored in Section 4.1.1. We used the simulations from the pixelised diffuse sky

¹⁵ <https://arrayfire.org>

¹⁶ <https://icl.utk.edu/magma/>

models to demonstrate the fundamental limitation of the point-source approximation. In short, simulating from a long baseline and a coarse map resolution can lead to aliasing. This limitation is intrinsic to the point-source approximation, not specific to `matvis`. We recommend that the users keep this fact in mind and perform their own tests for their use-cases before running large simulations.

There are currently a few limitations to `matvis`: (i) it can only simulate drift-scan observations; (ii) it can only simulate unpolarised (Stoke I) sky models, although it works with polarised beams; and (iii) it cannot simulate a subset of the pairs of a given set of antennas, for example just the non-redundant baselines in HERA. One way to enable “tracking observations”, addressing limitation (i), is to perform an additional step that rephrases the output visibilities to a chosen phase centre. In terms of limitation (ii), in principle, the current scheme can simulate positive polarised sky models, but allowing negative polarised flux to fully solve (ii) would require modifications to Equation 5 due to the square root of the sky flux. Solving (iii) would require changing (or adding) how the visibility is computed in Equation 3 to support a partial antenna matrix. We welcome contributions from the community to add support for any of these features.

ACKNOWLEDGEMENTS

This material is based upon work supported by the National Science Foundation under grants #1636646 and #1836019 and institutional support from the HERA collaboration partners. This research is funded in part by the Gordon and Betty Moore Foundation through Grant GBMF5212 to the Massachusetts Institute of Technology. HERA is hosted by the South African Radio Astronomy Observatory, which is a facility of the National Research Foundation, an agency of the Department of Science and Innovation.

P. Kittiwisit acknowledges the financial assistance of the South African Radio Astronomy Observatory (SARAO; www.sarao.ac.za). This result is part of a project that has received funding from the European Research Council (ERC) under the European Union’s Horizon 2020 research and innovation programme (Grant agreement No. 948764; P. Bull). P. Bull and H. Garsden acknowledge support from STFC Grants ST/T000341/1 and ST/X002624/1. S. G. Murray has received funding from the European Union’s Horizon 2020 research and innovation programme under the Marie Skłodowska-Curie grant agreement No. 101067043. C. Cain is supported by the Beus Center for Cosmic Foundations. This work used Bridges-2 at the Pittsburgh Supercomputing Centre (PSC) through allocation PHY210042 from the Advanced Cyberinfrastructure Coordination Ecosystem: Services & Support (ACCESS) program, which is supported by National Science Foundation grants #2138259, #2138286, #2138307, #2137603, and #2138296. We acknowledge the use of the `ilifu` cloud computing facility – www.ilifu.ac.za, a partnership between the University of Cape Town, the University of the Western Cape, Stellenbosch University, Sol Plaatje University, the Cape Peninsula University of Technology and the South African Radio Astronomy Observatory. The `ilifu` facility is supported by contributions from the Inter-University Institute for Data Intensive Astronomy (IDIA - a partnership between the University of Cape Town, the University of Pretoria and the University of the Western Cape), the Computational Biology division at UCT and the Data Intensive Research Initiative of South Africa (DIRISA).

DATA AVAILABILITY

`matvis` and `hera_sim` have been developed or contributed by members of the HERA collaboration. `pyuvsim` and `pyuvdata` are developed and maintained by the Radio Astronomy Software Group (RASG). All packages mentioned are publicly available on GitHub (see Section 3 for details). Visibility files from Section 4 can be made available upon request to the corresponding author.

REFERENCES

- Aguirre, J. E., Murray, S. G., Pascua, R., Martinot, Z. E., Burba, J., Dillon, J. S., Jacobs, D. C., Kern, N. S., Kittiwisit, P., Kolopanis, M., Lanman, A., Liu, A., Whittle, L., Abdurashidova, Z., Alexander, P., Ali, Z. S., Balfour, Y., Beardsley, A. P., Bernardi, G., Billings, T. S., Bowman, J. D., Bradley, R. F., Bull, P., Carey, S., Carilli, C. L., Cheng, C., DeBoer, D. R., Dexter, M., de Lera Acedo, E., Ely, J., Ewall-Wice, A., Fagnoni, N., Fritz, R., Furlanetto, S. R., Gale-Sides, K., Glendenning, B., Gorthi, D., Greig, B., Grobbelaar, J., Haldy, Z., Hazelton, B. J., Hewitt, J. N., Hickish, J., Julius, A., Kerrigan, J., Kohn, S. A., La Plante, P., Lekalake, T., Lewis, D., MacMahon, D., Malan, L., Malmgren, C., Maree, M., Matsetela, E., Mesinger, A., Molewa, M., Morales, M. F., Mosiane, T., Neben, A. R., Nikolic, B., Parsons, A. R., Patra, N., Pieterse, S., Pober, J. C., Razavi-Ghods, N., Ringuelet, J., Robnett, J., Rosie, K., Santos, M. G., Sims, P., Singh, S., Smith, C., Syce, A., Thyagarajan, N., Williams, P. K. G., Zheng, H., & HERA Collaboration, 2022. Validation of the HERA Phase I Epoch of Reionization 21 cm Power Spectrum Software Pipeline, *ApJ*, **924**(2), 85.
- Astropy Collaboration, Robitaille, T. P., Tollerud, E. J., Greenfield, P., Droettboom, M., Bray, E., Aldcroft, T., Davis, M., Ginsburg, A., Price-Whelan, A. M., Kerzendorf, W. E., Conley, A., Crighton, N., Barbary, K., Muna, D., Ferguson, H., Grollier, F., Parikh, M. M., Nair, P. H., Unther, H. M., Deil, C., Woillez, J., Conseil, S., Kramer, R., Turner, J. E. H., Singer, L., Fox, R., Weaver, B. A., Zabalza, V., Edwards, Z. I., Azalee Bostroem, K., Burke, D. J., Casey, A. R., Crawford, S. M., Dencheva, N., Ely, J., Jenness, T., Labrie, K., Lim, P. L., Pierfederici, F., Pontzen, A., Ptak, A., Refsdal, B., Servillat, M., & Streicher, O., 2013. Astropy: A community Python package for astronomy, *A&A*, **558**, A33.
- Astropy Collaboration, Price-Whelan, A. M., Sipőcz, B. M., Günther, H. M., Lim, P. L., Crawford, S. M., Conseil, S., Shupe, D. L., Craig, M. W., Dencheva, N., Ginsburg, A., VanderPlas, J. T., Bradley, L. D., Pérez-Suárez, D., de Val-Borro, M., Aldcroft, T. L., Cruz, K. L., Robitaille, T. P., Tollerud, E. J., Ardelean, C., Babej, T., Bach, Y. P., Baccetti, M., Bakanov, A. V., Bamford, S. P., Barentsen, G., Barmby, P., Baumbach, A., Berry, K. L., Biscani, F., Boquien, M., Bostroem, K. A., Bouma, L. G., Brammer, G. B., Bray, E. M., Breytenbach, H., Buddelmeijer, H., Burke, D. J., Calderone, G., Cano Rodríguez, J. L., Cara, M., Cardoso, J. V. M., Cheedella, S., Copin, Y., Corrales, L., Crichton, D., D’Avella, D., Deil, C., Depagne, É., Dietrich, J. P., Donath, A., Droettboom, M., Earl, N., Erben, T., Fabbro, S., Ferreira, L. A., Finethy, T., Fox, R. T., Garrison, L. H., Gibbons, S. L. J., Goldstein, D. A., Gommers, R., Greco, J. P., Greenfield, P., Groener, A. M., Grollier, F., Hagen, A., Hirst, P., Homeier, D., Horton, A. J., Hosseinzadeh, G., Hu, L., Hunkeler, J. S., Ivezić, Ž., Jain, A., Jenness, T., Kanarek, G., Kendrew, S., Kern, N. S., Kerzendorf, W. E., Khvalko, A., King, J., Kirkby, D., Kulkarni, A. M., Kumar, A., Lee, A., Lenz, D., Littlefair, S. P., Ma, Z., Macleod, D. M., Mastropietro, M., McCully, C., Montagnac, S., Morris, B. M., Mueller, M., Mumford, S. J., Muna, D., Murphy, N. A., Nelson, S., Nguyen, G. H., Ninan, J. P., Nöthe, M., Ogaz, S., Oh, S., Parejko, J. K., Parley, N., Pascual, S., Patil, R., Patil, A. A., Plunkett, A. L., Prochaska, J. X., Rastogi, T., Reddy Janga, V., Sabater, J., Sakurikar, P., Seifert, M., Sherbert, L. E., Sherwood-Taylor, H., Shih, A. Y., Sick, J., Silbiger, M. T., Singanamalla, S., Singer, L. P., Sladen, P. H., Sooley, K. A., Sornarajah, S., Streicher, O., Teuben, P., Thomas, S. W., Tremblay, G. R., Turner, J. E. H., Terrón, V., van Kerkwijk, M. H., de la Vega, A., Watkins, L. L., Weaver, B. A., Whitmore, J. B., Woillez, J., Zabalza, V., & Astropy Contributors, 2018.

- The Astropy Project: Building an Open-science Project and Status of the v2.0 Core Package, *AJ*, **156**(3), 123.
- Astropy Collaboration, Price-Whelan, A. M., Lim, P. L., Earl, N., Starkman, N., Bradley, L., Shupe, D. L., Patil, A. A., Corrales, L., Brasseur, C. E., N'othé, M., Donath, A., Tollerud, E., Morris, B. M., Ginsburg, A., Vaher, E., Weaver, B. A., Tocknell, J., Jamieson, W., van Kerkwijk, M. H., Robitaille, T. P., Merry, B., Bachetti, M., Günther, H. M., Aldcroft, T. L., Alvarado-Montes, J. A., Archibald, A. M., B'odi, A., Bapat, S., Barntsen, G., Baz'án, J., Biswas, M., Boquien, M., Burke, D. J., Cara, D., Cara, M., Conroy, K. E., Conseil, S., Craig, M. W., Cross, R. M., Cruz, K. L., D'Eugenio, F., Dencheva, N., Devillepoix, H. A. R., Dietrich, J. P., Eigenbrot, A. D., Erben, T., Ferreira, L., Foreman-Mackey, D., Fox, R., Freij, N., Garg, S., Geda, R., Glattly, L., Gondhalekar, Y., Gordon, K. D., Grant, D., Greenfield, P., Groener, A. M., Guest, S., Gurovich, S., Handberg, R., Hart, A., Hatfield-Dodds, Z., Homeier, D., Hosseinzadeh, G., Jenness, T., Jones, C. K., Joseph, P., Kalmbach, J. B., Karamehmtoğlu, E., Kaluszyński, M., Kelley, M. S. P., Kern, N., Kerzendorf, W. E., Koch, E. W., Kulumani, S., Lee, A., Ly, C., Ma, Z., MacBride, C., Maljaars, J. M., Muna, D., Murphy, N. A., Norman, H., O'Steen, R., Oman, K. A., Pacifici, C., Pascual, S., Pascual-Granado, J., Patil, R. R., Perren, G. I., Pickering, T. E., Rastogi, T., Roulston, B. R., Ryan, D. F., Rykoff, E. S., Sabater, J., Sakurikar, P., Salgado, J., Sanghi, A., Saunders, N., Savchenko, V., Schwardt, L., Seifert-Eckert, M., Shih, A. Y., Jain, A. S., Shukla, G., Sick, J., Simpson, C., Singanamalla, S., Singer, L. P., Singhal, J., Sinha, M., SipHocz, B. M., Spitzer, L. R., Stansby, D., Streicher, O., Sumak, J., Swinbank, J. D., Taranu, D. S., Tewary, N., Tremblay, G. R., Val-Borro, M. d., Van Kooten, S. J., Vasović, Z., Verma, S., de Miranda Cardoso, J. V., Williams, P. K. G., Wilson, T. J., Winkel, B., Wood-Vasey, W. M., Xue, R., Yoachim, P., Zhang, C., Zonca, A., & Astropy Project Contributors, 2022. The Astropy Project: Sustaining and Growing a Community-oriented Open-source Project and the Latest Major Release (v5.0) of the Core Package, *apj*, **935**(2), 167.
- Barry, N. & Chokshi, A., 2022. The Role of the Instrumental Response in 21 cm Epoch of Reionization Power Spectrum Gridding Analyses, *ApJ*, **929**(1), 64.
- Barry, N., Hazelton, B., Sullivan, I., Morales, M. F., & Pober, J. C., 2016. Calibration requirements for detecting the 21 cm epoch of reionization power spectrum and implications for the SKA, *MNRAS*, **461**(3), 3135–3144.
- Bassett, N., Rapetti, D., Tauscher, K., Nhan, B. D., Bordenave, D. D., Hibbard, J. J., & Burns, J. O., 2021. Lost Horizon: Quantifying the Effect of Local Topography on Global 21 cm Cosmology Data Analysis, *ApJ*, **923**(1), 33.
- Cheng, C., Parsons, A. R., Kolopanis, M., Jacobs, D. C., Liu, A., Kohn, S. A., Aguirre, J. E., Pober, J. C., Ali, Z. S., Bernardi, G., Bradley, R. F., Carilli, C. L., DeBoer, D. R., Dexter, M. R., Dillon, J. S., Klima, P., MacMahon, D. H. E., Moore, D. F., Nunhokee, C. D., Walbrugh, W. P., & Walker, A., 2018. Characterizing Signal Loss in the 21 cm Reionization Power Spectrum: A Revised Study of PAPER-64, *ApJ*, **868**(1), 26.
- Choudhuri, S., Bull, P., & Garsden, H., 2021. Patterns of primary beam non-redundancy in close-packed 21 cm array observations, *MNRAS*, **506**(2), 2066–2088.
- Cohen, A., Fialkov, A., & Barkana, R., 2018. Charting the parameter space of the 21-cm power spectrum, *MNRAS*, **478**(2), 2193–2217.
- de Oliveira-Costa, A., Tegmark, M., Gaensler, B. M., Jonas, J., Landecker, T. L., & Reich, P., 2010. Global Sky Model (GSM): A Model of Diffuse Galactic Radio Emission from 10 MHz to 100 GHz, Astrophysics Source Code Library, record ascl:1011.010.
- Dillon, J. S. & Parsons, A. R., 2016. Redundant Array Configurations for 21 cm Cosmology, *ApJ*, **826**(2), 181.
- Fagnoni, N., de Lera Acedo, E., Drought, N., DeBoer, D. R., Riley, D., Razavi-Ghods, N., Carey, S., & Parsons, A. R., 2021. Design of the New Wideband Vivaldi Feed for the HERA Radio-Telescope Phase II, *IEEE Transactions on Antennas and Propagation*, **69**(12), 8143–8157.
- Gehlert, B. K., Jacobs, D. C., Bowman, J. D., Mahesh, N., Murray, S. G., Kolopanis, M., Beardsley, A. P., Abdurashidova, Z., Aguirre, J. E., Alexander, P., Ali, Z. S., Balfour, Y., Bernardi, G., Billings, T. S., Bradley, R. F., Bull, P., Burba, J., Carey, S., Carilli, C. L., Cheng, C., DeBoer, D. R., Dexter, M., de Lera Acedo, E., Dillon, J. S., Ely, J., Ewall-Wice, A., Fagnoni, N., Fritz, R., Furlanetto, S. R., Gale-Sides, K., Glendenning, B., Gorthi, D., Greig, B., Grobbelaar, J., Halday, Z., Hazelton, B. J., Hewitt, J. N., Hickish, J., Julius, A., Kern, N. S., Kerrigan, J., Kittiwisit, P., Kohn, S. A., Lanman, A., La Plante, P., Lekalake, T., Lewis, D., Liu, A., Ma, Y.-Z., MacMahon, D., Malan, L., Malgas, C., Maree, M., Martinot, Z. E., Matsetela, E., Mesinger, A., Molewa, M., Monsalve, R. A., Morales, M. F., Mosiane, T., Neben, A. R., Nikolic, B., Parsons, A. R., Pascua, R., Patra, N., Pieterse, S., Pober, J. C., Razavi-Ghods, N., Ringuelette, J., Robnett, J., Rosie, K., Santos, M. G., Sims, P., Smith, C., Syce, A., Tegmark, M., Thyagarajan, N., Williams, P. K. G., & Zheng, H., 2021. Effects of model incompleteness on the drift-scan calibration of radio telescopes, *MNRAS*, **506**(3), 4578–4592.
- Górski, K. M., Hivon, E., Banday, A. J., Wandelt, B. D., Hansen, F. K., Reinecke, M., & Bartelmann, M., 2005. HEALPix: A Framework for High-Resolution Discretization and Fast Analysis of Data Distributed on the Sphere, *ApJ*, **622**(2), 759–771.
- Hamaker, J. P., 2006. Understanding radio polarimetry. V. Making matrix self-calibration work: processing of a simulated observation, *A&A*, **456**(1), 395–404.
- Hamaker, J. P., Bregman, J. D., & Sault, R. J., 1996. Understanding radio polarimetry. I. Mathematical foundations, *A&AS*, **117**, 137–147.
- Hazelton, B. J., Jacobs, D. C., Pober, J. C., & Beardsley, A. P., 2017. pyuvdata: an interface for astronomical interferometric datasets in python, *The Journal of Open Source Software*, **2**(10), 140.
- Hurley-Walker, N., Callingham, J. R., Hancock, P. J., Franzen, T. M. O., Hindson, L., Kapińska, A. D., Morgan, J., Offringa, A. R., Wayth, R. B., Wu, C., Zheng, Q., Murphy, T., Bell, M. E., Dwarakanath, K. S., For, B., Gaensler, B. M., Johnston-Hollitt, M., Lenc, E., Procopio, P., Staveley-Smith, L., Ekers, R., Bowman, J. D., Briggs, F., Cappallo, R. J., Deshpande, A. A., Greenhill, L., Hazelton, B. J., Kaplan, D. L., Lonsdale, C. J., McWhirter, S. R., Mitchell, D. A., Morales, M. F., Morgan, E., Oberoi, D., Ord, S. M., Prabu, T., Shankar, N. U., Srivani, K. S., Subrahmanyam, R., Tingay, S. J., Webster, R. L., Williams, A., & Williams, C. L., 2017. GaLactic and Extragalactic All-sky Murchison Widefield Array (GLEAM) survey - I. A low-frequency extragalactic catalogue, *MNRAS*, **464**(1), 1146–1167.
- Jacobs, D. C., Burba, J., Bowman, J. D., Neben, A. R., Stinnett, B., Turner, L., Johnson, K., Busch, M., Allison, J., Leatham, M., Serrano Rodriguez, V., Denney, M., & Nelson, D., 2017. First Demonstration of ECHO: an External Calibrator for Hydrogen Observatories, *PASP*, **129**(973), 035002.
- Josaitis, A. T., Ewall-Wice, A., Fagnoni, N., & de Lera Acedo, E., 2022. Array element coupling in radio interferometry I: a semi-analytic approach, *MNRAS*, **514**(2), 1804–1827.
- Kern, N. S., Parsons, A. R., Dillon, J. S., Lanman, A. E., Fagnoni, N., & de Lera Acedo, E., 2019. Mitigating Internal Instrument Coupling for 21 cm Cosmology. I. Temporal and Spectral Modeling in Simulations, *ApJ*, **884**(2), 105.
- Kern, N. S., Parsons, A. R., Dillon, J. S., Lanman, A. E., Liu, A., Bull, P., Ewall-Wice, A., Abdurashidova, Z., Aguirre, J. E., Alexander, P., Ali, Z. S., Balfour, Y., Beardsley, A. P., Bernardi, G., Bowman, J. D., Bradley, R. F., Burba, J., Carilli, C. L., Cheng, C., DeBoer, D. R., Dexter, M., de Lera Acedo, E., Fagnoni, N., Fritz, R., Furlanetto, S. R., Glendenning, B., Gorthi, D., Greig, B., Grobbelaar, J., Halday, Z., Hazelton, B. J., Hewitt, J. N., Hickish, J., Jacobs, D. C., Julius, A., Kerrigan, J., Kittiwisit, P., Kohn, S. A., Kolopanis, M., La Plante, P., Lekalake, T., MacMahon, D., Malan, L., Malgas, C., Maree, M., Martinot, Z. E., Matsetela, E., Mesinger, A., Molewa, M., Morales, M. F., Mosiane, T., Murray, S. G., Neben, A. R., Parsons, A. R., Patra, N., Pieterse, S., Pober, J. C., Razavi-Ghods, N., Ringuelette, J., Robnett, J., Rosie, K., Sims, P., Smith, C., Syce, A., Thyagarajan, N., Williams, P. K. G., & Zheng, H., 2020. Mitigating Internal Instrument Coupling for 21 cm Cosmology. II. A Method Demonstration with the Hydrogen Epoch of Reionization Array, *ApJ*, **888**(2), 70.
- Kohn, S. A., Aguirre, J. E., La Plante, P., Billings, T. S., Chichura, P. M., Fortino, A. F., Igarashi, A. S., Benéfó, R. K., Gallardo, S., Martinot, Z. E., Nunhokee, C. D., Kern, N. S., Bull, P., Liu, A., Alexander, P.,

- Ali, Z. S., Beardsley, A. P., Bernardi, G., Bowman, J. D., Bradley, R. F., Carilli, C. L., Cheng, C., DeBoer, D. R., de Lera Acedo, E., Dillon, J. S., Ewall-Wice, A., Fadana, G., Fagnoni, N., Fritz, R., Furlanetto, S. R., Glendenning, B., Greig, B., Grobelaar, J., Hazelton, B. J., Hewitt, J. N., Hickish, J., Jacobs, D. C., Julius, A., Kariseb, M., Kolopanis, M., Lekalake, T., Loots, A., MacMahon, D., Malan, L., Malgas, C., Maree, M., Mathison, N., Matsetela, E., Mesinger, A., Morales, M. F., Neben, A. R., Nikolic, B., Parsons, A. R., Patra, N., Pieterse, S., Pober, J. C., Razavi-Ghods, N., Ringuelet, J., Robnett, J., Rosie, K., Sell, R., Smith, C., Syce, A., Tegmark, M., Thyagarajan, N., Williams, P. K. G., & Zheng, H., 2019. The HERA-19 Commissioning Array: Direction-dependent Effects, *ApJ*, **882**(1), 58.
- Kolopanis, M., Jacobs, D. C., Cheng, C., Parsons, A. R., Kohn, S. A., Pober, J. C., Aguirre, J. E., Ali, Z. S., Bernardi, G., Bradley, R. F., Carilli, C. L., DeBoer, D. R., Dexter, M. R., Dillon, J. S., Kerrigan, J., Klima, P., Liu, A., MacMahon, D. H. E., Moore, D. F., Thyagarajan, N., Nunhokee, C. D., Walbrugh, W. P., & Walker, A., 2019. A Simplified, Lossless Reanalysis of PAPER-64, *ApJ*, **883**(2), 133.
- Lanman, A., Hazelton, B., Jacobs, D., Kolopanis, M., Pober, J., Aguirre, J., & Thyagarajan, N., 2019. Pyuvsim: A comprehensive simulation package for radio interferometers in python., *The Journal of Open Source Software*, **4**, 1234.
- Lanman, A. E. & Kern, N., 2019. healvis: Radio interferometric visibility simulator based on HEALpix maps, Astrophysics Source Code Library, record ascl:1907.002.
- Lanman, A. E., Murray, S. G., & Jacobs, D. C., 2022. Validation Solutions to the Full-sky Radio Interferometry Measurement Equation for Diffuse Emission, *ApJS*, **259**(1), 22.
- Le Gall, F. & Urrutia, F., 2017. Improved Rectangular Matrix Multiplication using Powers of the Coppersmith-Winograd Tensor, *arXiv e-prints*, p. arXiv:1708.05622.
- Martinot, Z. E., 2022. *Improvements in Interferometric Data Modeling for the New Era of Radio Cosmology*, Ph.D. thesis, University of Pennsylvania, Dissertations available from ProQuest, AAI29169424.
- McKinley, B., Yang, R., López-Cañego, M., Briggs, F., Hurley-Walker, N., Wayth, R. B., Offringa, A. R., Crocker, R., Bernardi, G., Procopio, P., Gaensler, B. M., Tingay, S. J., Johnston-Hollitt, M., McDonald, M., Bell, M., Bhat, N. D. R., Bowman, J. D., Cappallo, R. J., Corey, B. E., Deshpande, A. A., Emrich, D., Ewall-Wice, A., Feng, L., Goeke, R., Greenhill, L. J., Hazelton, B. J., Hewitt, J. N., Hindson, L., Jacobs, D., Kaplan, D. L., Kasper, J. C., Kratzenberg, E., Kudryavtseva, N., Lenc, E., Lonsdale, C. J., Lynch, M. J., McWhirter, S. R., Mitchell, D. A., Morales, M. F., Morgan, E., Oberoi, D., Ord, S. M., Pindor, B., Prabu, T., Riding, J., Rogers, A. E. E., Roshi, D. A., Udaya Shankar, N., Srivani, K. S., Subrahmanyan, R., Waterson, M., Webster, R. L., Whitney, A. R., Williams, A., & Williams, C. L., 2015. Modelling of the spectral energy distribution of Fornax A: leptonic and hadronic production of high-energy emission from the radio lobes, *MNRAS*, **446**(4), 3478–3491.
- Mort, B. J., Dulwich, F., Salvini, S., Adami, K. Z., & Jones, M. E., 2010. Oskar: Simulating digital beamforming for the ska aperture array, in *2010 IEEE International Symposium on Phased Array Systems and Technology*, pp. 690–694, IEEE.
- Noordam, J. E. & Smirnov, O. M., 2010. The MeqTrees software system and its use for third-generation calibration of radio interferometers, *A&A*, **524**, A61.
- Pagano, M., Liu, J., Liu, A., Kern, N. S., Ewall-Wice, A., Bull, P., Pascua, R., Ravanbakhsh, S., Abdurashidova, Z., Adams, T., Aguirre, J. E., Alexander, P., Ali, Z. S., Baartman, R., Balfour, Y., Beardsley, A. P., Bernardi, G., Billings, T. S., Bowman, J. D., Bradley, R. F., Burba, J., Carey, S., Carilli, C. L., Cheng, C., DeBoer, D. R., de Lera Acedo, E., Dexter, M., Dillon, J. S., Eksteen, N., Ely, J., Fagnoni, N., Fritz, R., Furlanetto, S. R., Gale-Sides, K., Glendenning, B., Gorthi, D., Greig, B., Grobelaar, J., Haldy, Z., Hazelton, B. J., Hewitt, J. N., Hickish, J., Jacobs, D. C., Julius, A., Kariseb, M., Kerrigan, J., Kittiwisit, P., Kohn, S. A., Kolopanis, M., Lanman, A., La Plante, P., Loots, A., MacMahon, D. H. E., Malan, L., Malgas, C., Malgas, K., Marero, B., Martinot, Z. E., Mesinger, A., Molewa, M., Morales, M. F., Mosiane, T., Neben, A. R., Nikolic, B., Nuwegeld, H., Parsons, A. R., Patra, N., Pieterse, S., Razavi-Ghods, N., Robnett, J., Rosie, K., Sims, P., Smith, C., Swarts, H., Thyagarajan, N., van Wyngaarden, P., Williams, P. K. G., & Zheng, H., 2023. Characterization of inpair residuals in interferometric measurements of the epoch of reionization, *MNRAS*, **520**(4), 5552–5572.
- Parsons, A. R., Liu, A., Ali, Z. S., & Cheng, C., 2016. Optimized Beam Sculpting with Generalized Fringe-rate Filters, *ApJ*, **820**(1), 51.
- Perkins, S. J., Marais, P. C., Zwart, J. T. L., Natarajan, I., Tasse, C., & Smirnov, O., 2015. Montblanc¹: GPU accelerated radio interferometer measurement equations in support of Bayesian inference for radio observations, *Astronomy and Computing*, **12**, 73–85.
- Price, D. C., 2016. PyGSM: Python interface to the Global Sky Model, Astrophysics Source Code Library, record ascl:1603.013.
- Price, D. C. & Smirnov, O. M., 2015. Generalized formalisms of the radio interferometer measurement equation, *MNRAS*, **449**(1), 107–118.
- Santos, M. G., Cooray, A., & Knox, L., 2005. Multifrequency Analysis of 21 Centimeter Fluctuations from the Era of Reionization, *ApJ*, **625**(2), 575–587.
- Smirnov, O. M., 2011. Revisiting the radio interferometer measurement equation. I. A full-sky Jones formalism, *A&A*, **527**, A106.
- Sullivan, I. S., Morales, M. F., Hazelton, B. J., Arcus, W., Barnes, D., Bernardi, G., Briggs, F. H., Bowman, J. D., Bunton, J. D., Cappallo, R. J., Corey, B. E., Deshpande, A., deSouza, L., Emrich, D., Gaensler, B. M., Goeke, R., Greenhill, L. J., Herne, D., Hewitt, J. N., Johnston-Hollitt, M., Kaplan, D. L., Kasper, J. C., Kincaid, B. B., Koenig, R., Kratzenberg, E., Lonsdale, C. J., Lynch, M. J., McWhirter, S. R., Mitchell, D. A., Morgan, E., Oberoi, D., Ord, S. M., Pathikulangara, J., Prabu, T., Remillard, R. A., Rogers, A. E. E., Roshi, A., Salah, J. E., Sault, R. J., Udaya Shankar, N., Srivani, K. S., Stevens, J., Subrahmanyan, R., Tingay, S. J., Wayth, R. B., Waterson, M., Webster, R. L., Whitney, A. R., Williams, A., Williams, C. L., & Wyithe, J. S. B., 2012. Fast Holographic Deconvolution: A New Technique for Precision Radio Interferometry, *ApJ*, **759**(1), 17.
- THE CASA TEAM, Bean, B., Bhatnagar, S., Castro, S., Donovan Meyer, J., Emonts, B., Garcia, E., Garwood, R., Golap, K., Gonzalez Villalba, J., Harris, P., Hayashi, Y., Hoskins, J., Hsieh, M., Jagannathan, P., Kawasaki, W., Keimpema, A., Kettens, M., Lopez, J., Marvil, J., Masters, J., Mc-Nichols, A., Mehringer, D., Miel, R., Moellenbrock, G., Montesino, F., Nakazato, T., Ott, J., Petry, D., Pokorny, M., Raba, R., Rau, U., Schiebel, D., Schweighart, N., Sekhar, S., Shimada, K., Small, D., Steeb, J.-W., Sugimoto, K., Suoranta, V., Tsutsumi, T., van Bemmell, I. M., Verkouter, M., Wells, A., Xiong, W., Szomoru, A., Griffith, M., Glendenning, B., & Kern, J., in press. CASA, the Common Astronomy Software Applications for Radio Astronomy, *PASP*.
- Vassilevska Williams, V., Xu, Y., Xu, Z., & Zhou, R., 2023. New Bounds for Matrix Multiplication: from Alpha to Omega, *arXiv e-prints*, p. arXiv:2307.07970.
- Wilensky, M. J., Morales, M. F., Hazelton, B. J., Star, P. L., Barry, N., Byrne, R., Jordan, C. H., Jacobs, D. C., Pober, J. C., & Trott, C. M., 2023. Evidence of Ultrafaint Radio Frequency Interference in Deep 21 cm Epoch of Reionization Power Spectra with the Murchison Wide-field Array, *ApJ*, **957**(2), 78.
- Zonca, A., Singer, L., Lenz, D., Reinecke, M., Rosset, C., Hivon, E., & Gorski, K., 2019. healpy: equal area pixelization and spherical harmonics transforms for data on the sphere in python, *Journal of Open Source Software*, **4**(35), 1298.

APPENDIX A: UTILISING BASELINE REDUNDANCIES

Let the matrix \mathbf{Z} have shape $N \times M$, where $N = N_{\text{feed}}N_{\text{ant}}$ and $M = N_{\text{ax}}N_{\text{src}}$. Then the matrix $\mathbf{V} = \mathbf{Z}\mathbf{Z}^\dagger$ has shape $N \times N$. As discussed in Section 5.3, one of the disadvantages of the current `matvis` implementation is that all N^2 antenna-feed pairs must be simulated, including those that are ‘redundant’.

To be clear, this redundancy occurs when two baselines, ij and kl , have equivalent beams and baseline vectors ($\mathbf{b}_{ij} = \mathbf{b}_{kl}$). We can split the baselines of any array into a number N'_u of sets of baselines, where each set contains all n_i baselines that are redundant with each

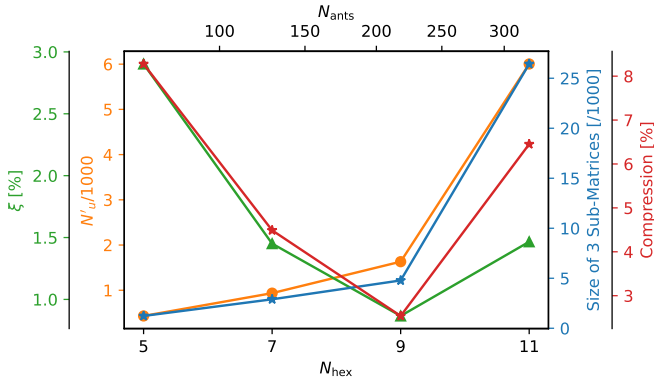


Figure A1. Characteristics of the ‘HERA-like’ arrays used in this appendix. The x-axis denotes the size of the array, defined by N_{hex} (the number of antennas along a side of the hexagon) and N_{ants} . The orange and green curves (left spines) show characteristics of the arrays: the number of unique pairs (orange) and the non-redundancy fraction, ξ . The blue and red curves (right spines) show indicate properties of the sub-matrix algorithm outlined in this appendix: the total size of the sub-matrices (in this case, 3 sub-matrices were used) in blue, and this size as a fraction of the full matrix. Unique pairs grow almost linearly with N_{ants} .

other, such that $\sum_i n_i = N_{\text{ant}}(N_{\text{ant}} + 1)/2$ (the sets don’t contain reverse-pairs since their visibilities are simply the conjugate of the reverse). Letting $N_u = N_{\text{feed}}^2 N'_u$ be the number of non-redundant elements of \mathbf{V} , we can write the ‘non-redundancy fraction’,

$$\xi = N_u / N^2, \quad (\text{A1})$$

which is very low for highly-redundant compact arrays like HERA. Thus, calculating the full N^2 matrix is performing far more calculations than strictly necessary.

In this appendix, we consider a few alternative approaches aimed at improving performance in this situation. Far from being a fully-fledged examination, we will limit our focus to a few ideas, and test their performance only on ‘HERA-like’ arrays, by which we mean that the antennas are arranged in a hexagonal core, split into three parallelogram shards (reducing redundancy) with N_{hex} antennas along a side. In this setup, ξ varies between ~ 1 -3%, and N'_u varies between 500-6000 (see Figure A1).

Figure A2 shows in blue the performance of the default implementation of `matvis`: the full matrix-matrix (MM) calculation. On the LHS the performance as a function of N_{ant} is shown, and on the RHS as a function of N_{src} . The black-dashed line is an indication of linear scaling with each parameter, whereas the black-dotted line indicates scaling with N_{ant}^2 . It is clear that the GPU implementation used here scales close to N_{ant}^2 .

The most straightforward way to use the redundancy of the array is to compute only the N_u vector-vector (VV) dot products required within a for-loop. This has complexity $O(N_u M \equiv \xi N^2 M)$, which is better than the $O(N^2 M)$ that the full matrix-matrix calculation exhibits in Figure A2. On the other hand, we expect this to have some overhead associated with the for-loop, and this is borne out in Figure A2, where this method is shown in green. For small N_{ant} , the overhead associated with the for-loop is large enough that this method is $\sim 6\times$ slower than the MM method. However, it grows with N_u instead of N^2 , which in the HERA-like case considered here is close to $N_u \propto N$. For the full HERA array, the VV loop is more performant than the MM calculation. Considering the performance against N_{src} , the VV loop has very poor performance for small N_{src} ,

and only starts to hit the theoretical linear growth for $N_{\text{src}} \gg 10^6$. This must be due to low utilisation of the many GPU cores: each VV dot product is performing N_{src} calculations split between thousands of cores.

A more general alternative approach is to deconstruct \mathbf{V} into a set of smaller matrices $\{\mathbf{V}'_x\}$, for which each \mathbf{V}'_x contains some non-zero number of unique pairs in \mathbf{V} , and is a smaller yet large enough matrix to take advantage of modern matrix multiplication routines,

$$\mathbf{V}'_x = \mathbf{A}_x \mathbf{B}_x^\dagger. \quad (\text{A2})$$

Here, \mathbf{A}_x and \mathbf{B}_x are both formed from (possibly non-adjacent) full rows of \mathbf{Z} , having shape $N_A \times M$ and $N_B \times M$ respectively. The rows chosen for \mathbf{B}_x correspond to the columns of \mathbf{V}'_x . We can then attempt to optimise the sets $\{\mathbf{A}_x\}$ and $\{\mathbf{B}_x\}$ to yield the best possible computation time for $\{\mathbf{V}'_x\}$ (and thus for \mathbf{V}) given a particular set of unique antenna pairs. This optimisation is obviously dependent on the antenna distribution. Note that both the vector dot-product approach described above and the full matrix product $\mathbf{V} = \mathbf{Z}\mathbf{Z}^\dagger$ are special cases of Equation A2, where the number of matrices in $\{\mathbf{V}'_x\}$ is N_u and 1, respectively.

For the full HERA array, the number of possible choices for $\{\mathbf{V}'_x\}$ is extremely large (since $N = 700$)¹⁷, which makes Equation A2 a daunting optimisation problem. However, the structure of the matrix can potentially lead to some useful ideas.

One such intermediate idea is for each \mathbf{A}_x to be a $1 \times M$ matrix, and each \mathbf{B}_x to include only the antennas for which the single antenna in \mathbf{A}_x appears in non-redundant pairs. This computes *only* the redundant pairs, like the VV method above. However, it is liable to utilise vectorisation better than the VV approach as it includes fewer but larger matrix-vector (MV) products. On the other hand, memory management may be a problematic overhead in this approach since for each of the N MV products, the matrix needs to be ‘formed’ by coalescing memory from non-adjacent rows in the full \mathbf{Z} matrix. This is borne out in Figure A2, where this method is shown in orange. While the scaling of the MV method with both N_{ant} and N_{src} is what we expect (and is therefore better than MM for some large N where ξ is very small), it is much slower than all the other methods, due to both the overhead in the for-loop (N_{ant} iterations are required) and in the movement of data on the GPU to form \mathbf{B}_x .

A more generic idea to optimise the choice of $\{\mathbf{A}_x\}$ and $\{\mathbf{B}_x\}$ is to place down sub-matrices that cover all unique entries of \mathbf{V} , but are as small as possible in size. A heuristic algorithm for this is the following:

- (i) Form a list of pairs of antennas, $\mathcal{U} = [(a_1, b_1), (a_2, b_2), \dots, (a_{N_u}, b_{N_u})]$ where each pair is a representative from one of the ‘redundant groups’. Since the choice of representative is arbitrary, there are many ways to do this, but one simple way is to use the first pair of the group in lexicographic order.
- (ii) Let $\alpha = \{a_1, a_2, \dots\}$ be the set of all ‘first’ antennas in \mathcal{U} , and β the corresponding set of ‘second’ antennas. Let N_α be the set of multiplicities of a_x in \mathcal{U} .
- (iii) Obtain α' , which is a list of the elements of α , sorted in descending order of their multiplicity. That is, sort antennas in decreasing order of how many times they appear as first-antenna in a unique pair.
- (iv) Decide on a number N_{sub} of sub-matrices into which \mathbf{V} should be partitioned: our partition will be limited to an ordered partition

¹⁷ There are N_u choices of *number* of matrices in the set, and for each such choice there a multitude of ways to configure the shape of each sub-matrix.

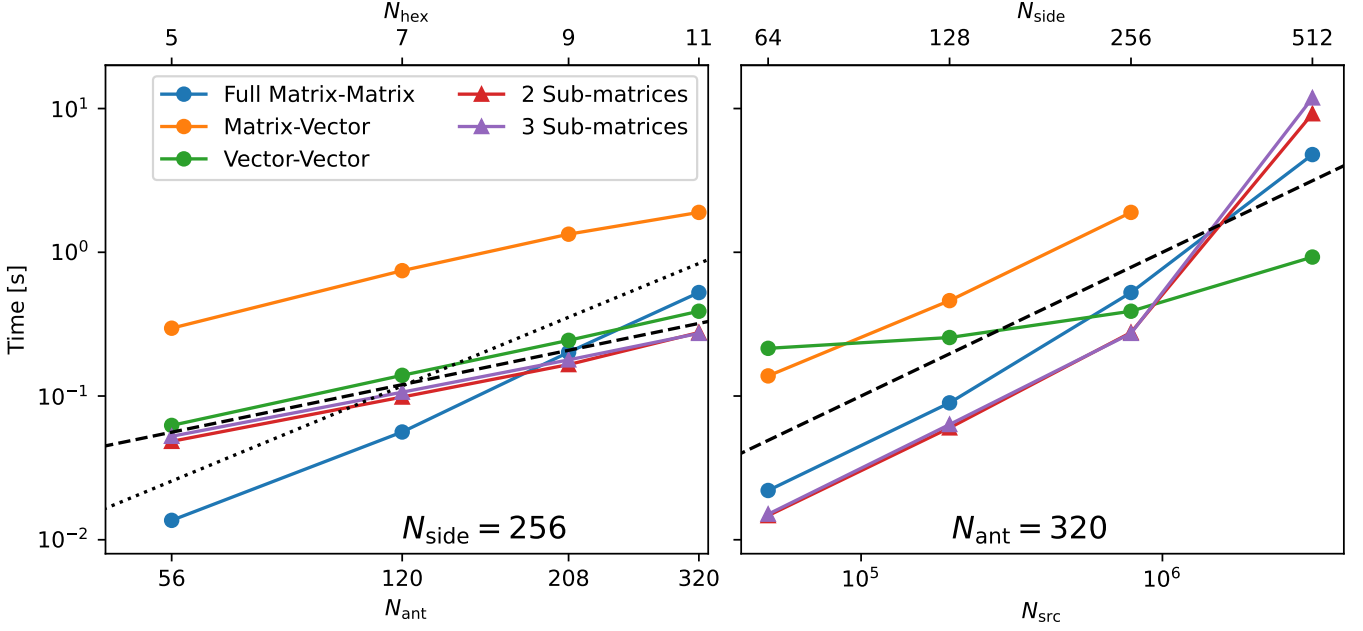


Figure A2. Performance characteristics of four different approaches to calculating \mathbf{V} . The LHS panel shows performance as a function of N_{ant} , where the array is a ‘HERA-like’ array with characteristics shown in Figure A1. Here $N_{\text{side}} = 256$ is used. On the RHS, N_{ant} is fixed at 320 and the performance as a function of N_{src} is shown. The full matrix-matrix method adopted by `matvis` is in blue, the matrix-vector approach in orange, the vector-vector dot product approach in green, and the more general sub-matrix approach in red and purple (for different numbers of sub-matrices). Black dashed line indicates linear scaling, and black dotted indicates quadratic scaling.

of α' , i.e. the placement of $N_{\text{sub}} - 1$ cuts in α' such that we have a new set of sub-lists, $\{\alpha'_x\}$, for $0 \leq x < N_{\text{sub}}$. Let the size of each subset be n_x , so that $\sum_x n_x = |\alpha|$; then α'_0 corresponds to the first n_0 values in α' , α'_1 the next n_1 values, etc. This defines the set $\{\mathbf{A}_x\}$ such that each element is the matrix formed by taking the rows of \mathbf{Z} corresponding to the indices in α'_x . Moreover, it uniquely defines the corresponding set $\{\beta_x\}$ which must be the set of all b_i that exist in a pair in \mathcal{U} where the first element is in α'_x . The set $\{\mathbf{B}_x\}$ is the analogue of $\{\mathbf{A}_x\}$ for $\{\beta_x\}$. Letting \mathcal{V}_x be the outer-product of pairs from α'_x and β'_x , $\mathcal{V}_x = \{(i, j) \mid i \in \alpha'_x, \forall j \in \beta_x\}$, we denote the ‘size’ of a particular sub-matrix as $S_x = |\mathcal{V}_x|$, and its ‘density’ \mathcal{D}_x is the ratio of the number of unique pairs in \mathcal{U} that appear in \mathcal{V}_x to S_x , i.e. $\mathcal{D}_x = |\mathcal{U} \cap \mathcal{V}_x| / |\mathcal{V}_x|$.

(v) To decide where the $N_{\text{sub}} - 1$ partitions should be placed, use an iterative procedure. First, notice that increasing the size of a sub-matrix \mathbf{A}_x by including one extra index from α' is almost always going to reduce the density \mathcal{D}_x , since α' is ordered by multiplicity. Using this, we simply do the following: for each partition point, defined by n_x , try all values from $n_x = 1, 2, \dots$, each time computing \mathcal{D}_x . Once \mathcal{D}_x reduces below a threshold τ , move to the next cut, n_{x+1} and do the same. After placing all cuts, compute $\mathcal{D}_{N_{\text{sub}}}$ for the last sub-matrix. If it is greater than τ , then we’re done. If not, reduce τ by some pre-defined small amount, and redo the loop over x with the new threshold.

The output of this algorithm is the ordered list α' and the set of cuts, $\{n_1, n_2, \dots, n_{N_{\text{sub}}}\}$, such that the densities \mathcal{D}_x are as high as possible while all remaining similar. Since computation time will scale roughly as the total size, $\mathcal{S} = \sum_x S_x$, we note that $\mathcal{S} = N_u / \mathcal{D}$, where by construction $\mathcal{D} < \min\{\mathcal{D}_x\}$. This process is illustrated in Figure A3. This algorithm is by no means guaranteed to return the best possible decomposition of \mathbf{V} : it is constrained to partitions only

in α' , not the joint space of α' and β (in the visual representation of Figure A2, different sub-matrices never appear on the same row), and it does not attempt to use other pairs from the redundant groups instead of the arbitrarily chosen representative pair. Nevertheless, it obviously does reasonably well in the case of HERA, with a compression factor of more than 15 for 3 sub-matrices compared to the full calculation. A trivial adaptation to the method is to reverse the pairs (i.e. pass (b, a) into the algorithm instead of (a, b)). Our tests show a compression factor of ~ 25 in this case.

Figure A2 shows the results of this sub-matrix method in red and purple (triangles), for 2- and 3-sub-matrices respectively. We firstly note that these two decompositions yield very similar performance. Overall they scale as we would expect: linearly with N_{ant} like the other methods that utilise redundancy, and linearly with N_{src} . Since each of the sub-matrices is reasonably large, we do not see issues of under-utilisation of the GPU parallelisation for small number of sources, like we did in the VV method.

The strongest downside to this method is that, similar to the MV method, it needs to copy memory on the GPU to form the \mathbf{A}_x and \mathbf{B}_x . Our tests show that this memory copying constitutes about 1/3 of the total runtime in our non-optimised implementation. Better memory management could make this method even more competitive. This is seen also in the $N_{\text{side}} = 512$ case, where there is a sudden jump in runtime. This is due to the extra memory consumption of this method; to get around this, a loop over chunks of N_{src} is required, with the extra memory copies associated. The sub-matrix method may also not work when baselines are not perfectly redundant since matrix compression utilise redundancies. We plan to improve on the method and conduct thorough tests before adding it to `matvis` in the near future.

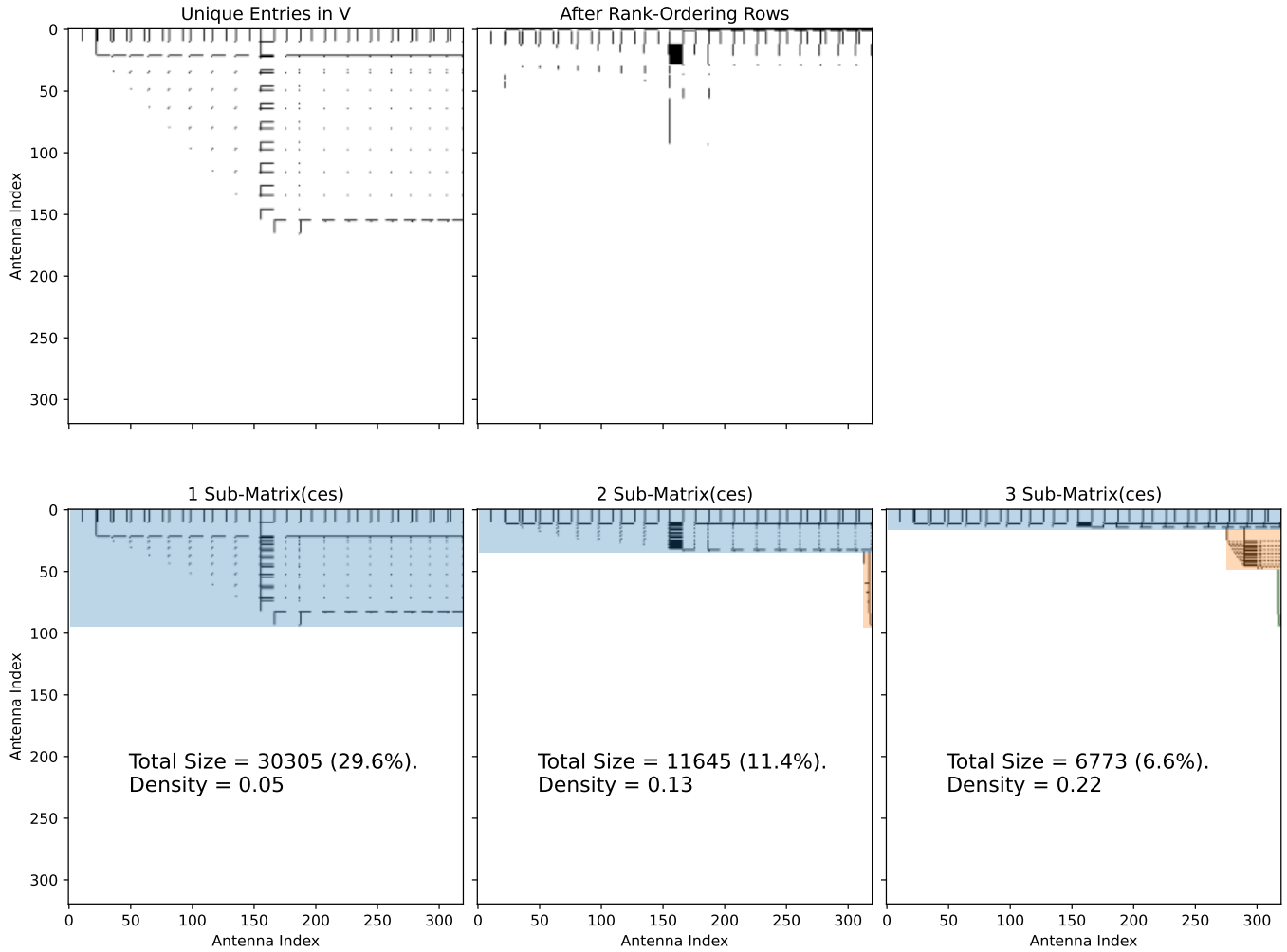


Figure A3. A visualisation of our sub-matrix procedure for taking advantage of antenna-pair redundancies in HERA. The plot is meant to be read from top-left to bottom-right. The top-left represents \mathbf{V} for HERA-320, where black pixels indicate unique baselines. These black pixels are less than 3% of the pixels. In the top-right, the rows have been re-ordered such that the top row has the most black dots, and the bottom row the least. On the bottom panel, we show the result of our algorithm for partitioning the rows into different numbers of subsets (1, 2 and 3 from left to right). In each case, after deciding on a vertical extent for the matrix (coloured region), the columns *within* the matrix are shuffled such that columns occupied by any row within the matrix are moved to the right. This is simply to visually indicate the final matrix density. All black pixels must be covered by a sub-matrix. The coloured-shaded regions show the matrices $\{V_x\}$ that can be calculated faster than the full matrix product. See text for details.

APPENDIX B: AUTHOR AFFILIATIONS

¹ Department of Physics and Astronomy, University of Western Cape, Cape Town, 7535, South Africa

² Scuola Normale Superiore, 56126 Pisa, PI, Italy

³ School of Earth and Space Exploration, Arizona State University, Tempe, AZ

⁴ Queen Mary University London, London E1 4NS, UK

⁵ Jodrell Bank Centre for Astrophysics, University of Manchester, Manchester, M13 9PL, United Kingdom

⁶ Department of Astronomy, University of California, Berkeley, CA

⁷ South African Radio Astronomy Observatory, Black River Park, 2 Fir Street, Observatory, Cape Town, 7925, South Africa

⁸ Department of Physics and Astronomy, University of Pennsylvania, Philadelphia, PA

⁹ Cavendish Astrophysics, University of Cambridge, Cambridge, UK

¹⁰ Department of Physics, Winona State University, Winona, MN

¹¹ INAF-Istituto di Radioastronomia, via Gobetti 101, 40129

Bologna, Italy

¹² Department of Physics and Electronics, Rhodes University, PO Box 94, Grahamstown, 6140, South Africa

¹³ National Radio Astronomy Observatory, Charlottesville, VA

¹⁴ National Radio Astronomy Observatory, Socorro, NM 87801, USA

¹⁵ MIT Kavli Institute, Massachusetts Institute of Technology, Cambridge, MA

¹⁶ Department of Physics, Massachusetts Institute of Technology, Cambridge, MA

¹⁷ Centre for Strings, Gravitation and Cosmology, Department of Physics, Indian Institute of Technology Madras, Chennai 600036, India

¹⁸ Radio Astronomy Lab, University of California, Berkeley, CA

¹⁹ Department of Physics, University of California, Berkeley, CA

²⁰ Department of Physics and Astronomy, University of California, Los Angeles, CA

²¹ National Radio Astronomy Observatory, Socorro, NM

²² *Department of Physics and McGill Space Institute, McGill University, 3600 University Street, Montreal, QC H3A 2T8, Canada*

²³ *School of Physics, University of Melbourne, Parkville, VIC 3010, Australia*

²⁴ *Department of Physics, University of Washington, Seattle, WA*

²⁵ *eScience Institute, University of Washington, Seattle, WA*

[†] *NASA Hubble Fellow*

²⁶ *Department of Physics, Brown University, Providence, RI*

²⁷ *School of Chemistry and Physics, University of KwaZulu-Natal*

²⁸ *International Centre for Radio Astronomy Research, Curtin University, Bentley, WA 6102, Australia*

²⁹ *ARC Centre of Excellence for All Sky Astrophysics in 3 Dimensions (ASTRO 3D), Bentley, WA 6102, Australia*

³⁰ *School of Physics, University of Melbourne, Parkville, VIC 3010 Australia*

³¹ *Raman Research Institute*

³² *Commonwealth Scientific and Industrial Research Organisation (CSIRO), Space & Astronomy, P. O. Box 1130, Bentley, WA 6102, Australia*

³³ *Center for Astrophysics, Harvard & Smithsonian, Cambridge, MA*

³⁴ *American Astronomical Society, Washington, DC*

This paper has been typeset from a \TeX/L\AA\TeX file prepared by the author.